Monthly Notices of the ROYAL ASTRONOMICAL SOCIETY

MNRAS **530,** 1711–1731 (2024) https://doi.org/10.1093/mnras/stae824
Advance Access publication 2024 March 20

Accretion onto disc galaxies via hot and rotating CGM inflows

Jonathan Stern [1]★ Drummond Fielding [2] Zachary Hafen [3] Kung-Yi Su,[2] Nadav Naor,[1] Claude-André Faucher-Giguère [4] Eliot Quataert [5] and James Bullock [3]

[1]*School of Physics and Astronomy, Tel Aviv University, Tel Aviv 69978, Israel*
[2]*Center for Computational Astrophysics, Flatiron Institute, 162 Fifth Avenue, New York, NY 10010, USA*
[3]*Department of Physics and Astronomy, 4129 Reines Hall, University of California, Irvine, CA 92697, USA*
[4]*Department of Physics and Astronomy and CIERA, Northwestern University, 1800 Sherman Ave, Evanston, IL 60201, USA*
[5]*Department of Astrophysical Sciences, Princeton University, Princeton, NJ 08544, USA*

Accepted 2024 March 18. Received 2024 March 17; in original form 2023 May 31

ABSTRACT

Observed accretion rates onto the Milky Way and other local spirals fall short of that required to sustain star formation for cosmological timescales. A potential avenue for this unseen accretion is a rotating inflow in the volume-filling hot phase ($\sim 10^6$ K) of the circumgalactic medium (CGM), as suggested by some cosmological simulations. Using hydrodynamic simulations and a new analytic solution valid in the slow-rotation limit, we show that a hot inflow spins up as it approaches the galaxy, while remaining hot, subsonic, and quasi-spherical. Within the radius of angular momentum support (~ 15 kpc for the Milky Way) the hot flow flattens into a disc geometry and then cools from $\sim 10^6$ to $\sim 10^4$ K at the disc–halo interface. Cooling affects all hot gas, rather than just a subset of individual gas clouds, implying that accretion via hot inflows does not rely on local thermal instability in contrast with 'precipitation' models for galaxy accretion. Prior to cooling and accretion the inflow completes $\approx t_{\rm cool}/t_{\rm ff}$ radians of rotation, where $t_{\rm cool}/t_{\rm ff}$ is the cooling time to free-fall time ratio in hot gas immediately outside the galaxy. The ratio $t_{\rm cool}/t_{\rm ff}$ may thus govern the development of turbulence and enhancement of magnetic fields in gas accreting onto low-redshift spirals. We show that if rotating hot inflows are common in Milky-Way-size disc galaxies, as predicted, then signatures of the expected hot gas rotation profile should be observable with X-ray telescopes and fast radio burst surveys.

Key words: galaxies: disc – galaxies: evolution – galaxies: formation – galaxies: haloes – intergalactic medium.

1 INTRODUCTION

Observation of neutral gas surrounding the Milky Way and nearby spirals suggest accretion rates of 0.05–0.2 $\rm M_\odot\,yr^{-1}$, falling short of the 1–2 $\rm M_\odot\,yr^{-1}$ required to sustain observed star formation rates (SFRs) for cosmological timescales (Sancisi et al. 2008; Putman, Peek & Joung 2012; Kamphuis et al. 2022). This 'missing accretion' is often attributed to predominantly ionized gas clumps with temperature $\sim 10^4$ K (e.g. Voit et al. 2017), observable mainly in ultraviolet (UV) absorption. It is however unclear if this phase can provide the necessary fuel for star formation, due to both uncertainties in converting UV absorption features to net accretion rates (e.g. Fox et al. 2019), and since hydrodynamic instabilities may disrupt and evaporate cool gas clumps before they reach the galaxy (Heitsch & Putman 2009; Armillotta et al. 2017; Afruni et al. 2023; Tan, Oh & Gronke 2023). An alternative, less explored possibility is that accretion proceeds via a subsonic inflow in the volume-filling hot phase ($\sim 10^6$ K) of the circumgalactic medium (CGM), similar to classic 'cooling flow' solutions discussed in the context of the intracluster medium (ICM, Mathews & Bregman 1978; Fabian, Nulsen & Canizares 1984). Such hot CGM inflows are evident in modern cosmological simulations such as FIRE (Stern et al. 2021b; Hafen et al. 2022) and TNG (ZuHone et al. 2023; see also fig. 9 in Nelson et al. 2019).

Since the hot CGM is expected to have a net rotation (e.g. Roškar et al. 2010; Stevens et al. 2017; Oppenheimer 2018; DeFelippis et al. 2020; Huscher et al. 2021; Nica et al. 2022; Truong et al. 2021), an inflow will cause it to spin up. Stern et al. (2020) used an idealized 1-D model to show that in Milky Way mass haloes, such a rotating hot inflow will remain hot down to the radius where the rotation velocity approaches the circular velocity $v_{\rm c} = \sqrt{GM(<r)/r}$, at which point the gas cools to $\sim 10^4$ K and joins the ISM disc. Hafen et al. (2022) demonstrated that this picture applies, and is the dominant accretion mode onto $z \sim 0$ Milky Way mass galaxies in the FIRE-2 cosmological zoom simulations (Hopkins et al. 2018). They further showed that the flow forms a coherently spinning disc prior to accretion onto the galaxy, and that this coherence may be a necessary condition for the formation of thin disc galaxies, consistent with conclusions from related FIRE-2 analyses (Yu et al. 2021, 2023; Stern et al. 2021a, b; Gurvich et al. 2023). It thus appears that a deep understanding of the physics of hot and rotating inflows could be crucial for understanding the evolution of local star-forming discs.

In this paper, we complement the cosmological simulation-based analysis of hot and rotating CGM inflows in Hafen et al. (2022), by deriving an idealized, 2D axisymmetric solution for inflowing and

★ E-mail: sternjon@tauex.tau.ac.il

rotating hot CGM. Deriving an idealized solution allows identifying its dependence on system parameters and boundary conditions, and provides a basis for assessing the effects of additional physics. Our derivation is built on previous 1D hot inflow solutions,[1] which accounted for rotation in a highly approximate manner (Cowie, Fabian & Nulsen 1980; Birnboim & Dekel 2003; Narayan & Fabian 2011; Stern et al. 2020). These 1D studies assumed the centrifugal force is directed outward in the spherical radius direction, so the solution remained spherically symmetric. Here, we assume the centrifugal force is directed outward in the cylindrical radius direction, and derive a 2D axisymmetric solution which captures the transition from a quasi-spherical flow at large scales where rotational support is weak to a disc geometry at small scales where rotational support dominates. The idealized nature of our approach implies that insights may be applicable also to other astrophysical discs fed by spherical inflows, such as active galactic nucleus (AGN) discs in galaxy centres (e.g. Quataert & Narayan 2000) or protoplanetary discs in the centre of star-forming clouds (e.g. Fielding et al. 2015).

The inflowing hot CGM solution derived herein focuses on the limit where feedback heating is subdominant to radiatively cooling, thus differing qualitatively from radially static hot CGM models (also known as 'thermal balance' models, e.g. McCourt et al. 2012; Sharma et al. 2012a; Faerman, Sternberg & McKee 2017, 2020; Pezzulli, Fraternali & Binney 2017; Voit et al. 2017; Sormani et al. 2018), and from hot outflow models (Thompson et al. 2016; Schneider et al. 2020). Thermal balance models assume that radiative cooling is equal to feedback heating, thus inhibiting the hot inflow, while outflow models require that feedback heating dominates. Observational evidence for thermal balance is strong in the ICM, since the SFR at the cluster centre is small relative to the inflow rate $\dot{M}$ implied by the X-ray emission L_X. This is the well-known 'cooling flow problem', where $\dot{M} \approx L_X/v_c^2 \gg$ SFR (see McDonald et al. 2018, for a recent revisit). There is, however, no similar cooling flow problem in disc galaxies. Upper limits on L_X from the hot CGM of Milky Way mass galaxies are a few $\times 10^{40}$ erg s^{-1} (Li & Wang 2013; Li, Crain & Wang 2014; Anderson et al. 2015; Comparat et al. 2022), and recent results based on eROSITA data indicate the actual emission may be comparable to this value (Chadayammuri et al. 2022). For $v_c \approx 200$ km s^{-1} this L_X implies $\dot{M} \approx 1\,\mathrm{M}_\odot\,\mathrm{yr}^{-1} \sim$ SFR, in contrast with $\dot{M} \gg$ SFR deduced for the ICM. Similarly, estimates of $\dot{M}$ in the Milky Way halo suggest $\dot{M} \approx 0.1 - 1\,\mathrm{M}_\odot\,\mathrm{yr}^{-1}$ (Miller & Bregman 2015; Li & Bregman 2017; Stern et al. 2019), again inconsistent with the $\dot{M} \gg$ SFR derived for the ICM. More massive spirals in which the hot CGM is detected in individual objects with $L_X \gtrsim 10^{41}$ erg s^{-1} have SFR $\approx 10\,\mathrm{M}_\odot\,\mathrm{yr}^{-1}$ and hence also satisfy $\dot{M} \sim$ SFR (Anderson, Churazov & Bregman 2016; Bogdán et al. 2017; Das et al. 2019). A cooling flow problem akin to that in the ICM does not exist in the CGM of disc galaxies, allowing for the possibility that the hot CGM is inflowing.

The paper is organized as follows. In Section 2, we discuss the structure and properties of hot and rotating CGM using analytic considerations, while in Section 3, we derive a numerical solution. In Section 4, we consider the effect of additional physical mechanisms which were not included in the basic analysis, and in Section 5, we derive several observables of hot rotating CGM. Implications of our results are discussed in Section 6 and Section 7 provides a summary.

[1]Also called 'cooling flows' in the classic ICM literature, though note that this term has been used also to describe flows which cool out in halo (e.g. McQuinn & Werk 2018), rather than at the disc–halo interface. The hot rotating inflow solution in this paper can thus be described as a 'rotating cooling flow'.

2 THE STRUCTURE OF HOT AND ROTATING CGM – ANALYTIC CONSIDERATIONS

The flow equations for radiating, ideal gas with adiabatic index $\gamma = 5/3$ subject to an external gravitational potential Φ are

$$\nabla \cdot (\rho \boldsymbol{v}) = -\frac{\partial \rho}{\partial t}, \tag{1}$$

$$\left(\frac{\partial}{\partial t} + \boldsymbol{v} \cdot \nabla\right) \boldsymbol{v} = -\frac{1}{\rho}\nabla P - \nabla\Phi, \tag{2}$$

$$\left(\frac{\partial}{\partial t} + \boldsymbol{v} \cdot \nabla\right) \ln K = -\frac{1}{t_{\rm cool}}, \tag{3}$$

where ρ, P, and $\boldsymbol{v}$ are, respectively, the gas density, pressure, and velocity. We use $K \equiv P\rho^{-5/3}$ for the 'entropy' (up to an exponent and a constant) and $t_{\rm cool}$ for the cooling time, defined as

$$t_{\rm cool} = \frac{3}{2}\frac{P}{n_{\rm H}^2 \Lambda}\,, \tag{4}$$

where $n_{\rm H}$ is the hydrogen density, $(3/2)P$ is the energy per unit volume, and Λ is the cooling function defined such that $n_{\rm H}^2\Lambda$ is the energy lost to radiation per unit volume per unit time. Equations (1)–(3) neglect conduction, viscosity and magnetic fields, the potential effect of which will be assessed below. We also do not include a heating term in equation (3) since we search for a solution in the limit that heating is subdominant to cooling (see Introduction).

2.1 Hot CGM without angular momentum

We start with a brief review of steady-state ($\partial/\partial t = 0$) hot inflow solutions without angular momentum, which were studied extensively mainly in the context of the inner ICM (classic 'cooling flows', e.g. Mathews & Bregman 1978) and adapted to galaxy-scale haloes by Stern et al. (2019). When angular momentum is neglected spherical symmetry can be assumed, and hence equations (1)–(3) reduce to

$$4\pi r^2 \rho v_r = \dot{M}, \tag{5}$$

$$\frac{1}{2}v_r^2 = -\frac{1}{\rho}\frac{{\rm d}\left(P_{\rm th} + P_{\rm turb}\right)}{{\rm d}r} - \frac{v_c^2}{r}, \tag{6}$$

$$v_r \frac{{\rm d}\ln K}{{\rm d}r} = -\frac{1}{t_{\rm cool}}, \tag{7}$$

where r is the spherical radius, $\dot{M}$ is the mass flow rate (constant with radius in steady state, down to the radius where stars form), $P_{\rm turb} = \rho\sigma_{\rm turb}^2$ is the turbulent pressure, and $\sigma_{\rm turb}$ is the turbulent velocity. Multiplying both sides of equation (7) by the free-fall time $t_{\rm ff} = \sqrt{2}r/v_c$ (defined as in McCourt et al. 2012), we get

$$\frac{\sqrt{2}v_r}{v_c}\frac{{\rm d}\ln K}{{\rm d}\ln r} = -\frac{t_{\rm ff}}{t_{\rm cool}}\,. \tag{8}$$

This equation indicates that if $t_{\rm cool} \gg t_{\rm ff}$, then either the flow is isentropic with ${\rm d}\ln K/{\rm d}r \approx 0$ as in the Bondi (1952) solution, or that the inflow velocity is small, that is,

$$\frac{v_r}{v_c} \sim \left(\frac{t_{\rm cool}}{t_{\rm ff}}\right)^{-1} \ll 1\,. \tag{9}$$

The solutions discussed here correspond to the latter type of solutions where $v_r \ll v_c$, known as cooling flow solutions in the ICM literature. Hydrodynamic simulations show that initially static gas with $t_{\rm cool} \gg$

$t_{\rm ff}$ converges onto a cooling flow solution within a timescale $t_{\rm cool}$, rather than onto an isentropic flow (e.g. Stern et al. 2019).

To derive an analytic approximation, one can neglect in equation (6) the small inertial term v_r^2 and the turbulent term which is also expected to be small $P_{\rm turb} \sim (v_r/v_{\rm c})^2 P_{\rm th}$ (see Section 4.2 below). Further approximating the gravitational potential as isothermal with some constant $v_{\rm c}$ then gives (see section 2 in Stern et al. 2019):

$$\begin{aligned} c_{\rm s}^2 &= \frac{10}{9} v_{\rm c}^2, \\ T &= 2.0 \times 10^6 \, v_{\rm c,200}^2 \, {\rm K}, \\ n_{\rm H} &= 0.8 \times 10^{-3} \, r_{10}^{-1.5} v_{\rm c,200} \dot{M}_1^{0.5} \Lambda_{-22}^{-0.5} \, {\rm cm}^{-3}, \\ t_{\rm cool} &= 370 \, r_{10}^{1.5} v_{\rm c,200} \dot{M}_1^{-0.5} \Lambda_{-22}^{-0.5} \, {\rm Myr}, \\ -v_r = \frac{r}{t_{\rm cool}} &= 27 \, r_{10}^{-0.5} v_{\rm c,200}^{-1} \dot{M}_1^{0.5} \Lambda_{-22}^{0.5} \, {\rm km \, s^{-1}}, \\ -\mathcal{M}_r = \sqrt{\frac{9}{20}} \frac{t_{\rm ff}}{t_{\rm cool}} &= 0.13 \, r_{10}^{-0.5} v_{\rm c,200}^{-2} \dot{M}_1^{0.5} \Lambda_{-22}^{0.5}, \end{aligned} \tag{10}$$

where $c_{\rm s}$ is the sound speed, T is the temperature, $\mathcal{M}_r \equiv v_r/c_{\rm s}$ is the radial Mach number of the flow, and we normalized by the following numerical values: $r_{10} = r/10 \, {\rm kpc}$, $v_{\rm c,200} = v_{\rm c}/200 \, {\rm km \, s^{-1}}$, $\dot{M}_1 = \dot{M}/1 \, {\rm M_\odot \, yr^{-1}}$, and $\Lambda_{-22} = \Lambda/10^{-22} \, {\rm erg \, cm^3 \, s^{-1}}$. Equation (10) treats $\dot{M}$ as the free parameter, though one can also treat the CGM mass or density profile normalization as a free parameter, and then $\dot{M}$ follows from the density relation in equation (10).

The numerical values used in equation (10) are appropriate for the Milky Way CGM: $\dot{M}$ is taken to be roughly half the SFR of $\approx 1.5 - 2 \, {\rm M_\odot \, yr^{-1}}$ (Bland-Hawthorn & Gerhard 2016), as expected in steady state where the ISM mass is constant with time, and ≈ 40 per cent of the stellar mass formed is ejected back into the ISM via winds and supernovae (e.g. Lilly et al. 2013). This $\dot{M}$ is also consistent with X-ray absorption and emission constraints on the hot CGM of the Milky Way (see Introduction). The value of Λ is appropriate for $T = 2 \times 10^6 \, {\rm K}$ gas with metallicity $Z_\odot/3$, as measured for the Milky Way CGM (Miller & Bregman 2015). Equation (10) reveals several properties of the non-rotating solution. The inflow velocity v_r is equal to $r/t_{\rm cool}$, so the accretion time equals the cooling time, as expected in a cooling flow. This also implies that the entropy drops linearly with decreasing radius (see equation 7). Additionally, the inflow has a temperature which is independent of radius and roughly equal to the halo virial temperature, despite radiative losses. This is a result of compressive heating during the inflow balancing radiative cooling.

The solution in equation (10) also highlights that the parameter $t_{\rm cool}/t_{\rm ff}$ sets the Mach number of the flow, and thus also the sonic radius of the flow where $|\mathcal{M}_r| = 1$:

$$r_{\rm sonic} \approx r(t_{\rm cool} = 0.7 t_{\rm ff}) = 0.17 \, v_{\rm c,200}^{-4} \dot{M}_1 \Lambda_{-22} \, {\rm kpc} \, , \tag{11}$$

where we approximated $\sqrt{9/20} \approx 0.7$. Note that near and within the sonic radius the assumption of a quasi-hydrostatic flow is invalid, so the estimate of $r_{\rm sonic}$ is approximate. Equation (11) indicates that $r_{\rm sonic}$ is well within the galaxy for Milky Way parameters, though it can be on CGM scales in lower mass galaxies where $v_{\rm c}$ is lower, or at higher redshift where $\dot{M}$ is higher. In this paper, we focus on systems with $r_{\rm sonic}$ smaller than the galaxy scale, so the quasi-hydrostatic approximation is valid throughout the CGM.

Another important scale of cooling flows is the cooling radius $r_{\rm cool}$ at which $t_{\rm cool}$ equals the system age or the time since the last heating event. This scale is not part of the steady-state solution, since a cooling flow develops on a timescale $t_{\rm cool}$ and thus steady state is achieved only at $r < r_{\rm cool}$. A time-dependent solution for how the outer boundary of the inflow at $r \sim r_{\rm cool}$ expands as $r_{\rm cool}$ grows was derived by Bertschinger (1989). For the above parameters $t_{\rm cool} = 10 \, {\rm Gyr}$ occurs at $r = 110 \, {\rm kpc}$, so when necessary we assume $r_{\rm cool} = 100 \, {\rm kpc}$. The present study however focuses on smaller radii of $r \lesssim 40 \, {\rm kpc}$ where the dynamical effects of angular momentum are most pronounced, so $t_{\rm cool}$ is short relative to cosmological timescales and thus steady state is more likely to be achieved. This inner CGM region is also less susceptible to cosmological effects not included in our analysis, such as non-spherical accretion and satellite galaxies (Fielding et al. 2020).

2.2 Rotating hot CGM inflows – the circularization radius

Given some net angular momentum in the hot gas, for example due to torques applied by neighbouring haloes, the rotation velocity will increase as the gas inflows. We can hence define a circularization radius $R_{\rm c}$ as the radius where the rotational velocity equals the circular velocity and the flow becomes rotationally supported:

$$R_{\rm c} \equiv R(v_\phi = v_{\rm c}) \, , \tag{12}$$

where here and henceforth we use R for the cylindrical radius (and r for the spherical radius). One can also express $R_{\rm c}$ using the specific angular momentum of the hot gas j:

$$j = v_{\rm c}(R_{\rm c}) R_{\rm c} \, . \tag{13}$$

Cosmological considerations can be used to estimate a typical $R_{\rm c}$. In a ΛCDM cold dark matter universe, a given dark matter halo is expected to have a spin parameter λ which on average equals:

$$\lambda \equiv \frac{J}{\sqrt{2} M_{\rm vir} v_{\rm vir} r_{\rm vir}} \sim 0.035 \tag{14}$$

(e.g. Bullock et al. 2001; Rodríguez-Puebla et al. 2016), where $M_{\rm vir}$, $v_{\rm vir}$, $r_{\rm vir}$, and J correspond to the halo mass, virial velocity, virial radius, and angular momentum, correspondingly. Assuming the hot CGM has roughly the same spin as the dark matter halo as suggested by cosmological simulations (e.g. Stewart et al. 2013, 2017; DeFelippis et al. 2020; Hafen et al. 2022), and assuming that near the disc $v_{\rm c} = f_{v_{\rm c}} v_{\rm vir}$ with $f_{v_{\rm c}} \gtrsim 1$, we get

$$R_{\rm c} \approx \sqrt{2} \lambda \, f_{v_{\rm c}}^{-1} r_{\rm vir} \sim 15 \, f_{v_{\rm c}}^{-1} \left(\frac{r_{\rm vir}}{300 \, {\rm kpc}} \right) \, {\rm kpc} \, . \tag{15}$$

Comparison of equation (15) with equation (11) implies that $R_{\rm c} \gg r_{\rm sonic}$ in Milky Way haloes. Thus, a hot CGM inflow in a Milky Way halo is expected to become rotation-supported well before it transitions into a supersonic flow. This conclusion is also apparent if we estimate the radial Mach number near $R_{\rm c}$. Using equation (10), we have

$$\frac{t_{\rm cool}}{t_{\rm ff}}(R_{\rm c}) = 6.3 \left(\frac{R_{\rm c}}{15 \, {\rm kpc}} \right)^{0.5} v_{\rm c,200}^2 \dot{M}_1^{-0.5} \Lambda_{-22}^{-0.5} \, , \tag{16}$$

and hence

$$\mathcal{M}_r(R_{\rm c}) \approx 0.7 (t_{\rm cool}/t_{\rm ff})^{-1} \approx 0.1 \, . \tag{17}$$

The difference between CGM with $r_{\rm sonic} < R_{\rm c}$ and CGM with $r_{\rm sonic} > R_{\rm c}$ was discussed by Stern et al. (2020), and is related to the classic distinction between 'hot mode' and 'cold mode' accretion (White & Rees 1978; Birnboim & Dekel 2003; Fielding et al. 2017). In this paper, we focus on systems with $r_{\rm sonic} < R_{\rm c}$ so the hot accretion mode dominates.

2.3 Rotating hot CGM inflows – fluid equations and outer boundary condition

Accounting for angular momentum, and assuming steady state and axisymmetry, the r and θ components of the momentum equation (2) reduce to

$$\frac{\partial P}{\partial r} = -\rho\frac{v_c^2}{r} + \rho\Omega^2 r\sin^2\theta, \tag{18}$$

$$\frac{\partial P}{\partial \theta} = \rho\Omega^2 r^2\sin\theta\cos\theta, \tag{19}$$

where θ is the angle relative to the rotation axis and $\Omega = v_\phi/(r\sin\theta)$ is the angular frequency (v_r, v_θ, v_ϕ are the velocity vector components). We neglect the inertial v_r^2 term since its magnitude relative to the other terms is of order $\mathcal{M}_r^2 \approx (t_{\rm cool}/t_{\rm ff})^{-2}$. We similarly neglect the v_θ^2 and $v_r v_\theta$ terms, since motion in the θ direction is a result of the combination of radial and rotational motions, and hence v_θ is of the same order as v_r or smaller. The momentum equation in the ϕ direction is

$$v_r\frac{\partial}{\partial r}(\Omega r^2\sin^2\theta) = -v_\theta\frac{\partial}{r\partial\theta}(\Omega r^2\sin^2\theta)\,, \tag{20}$$

which indicates that the specific angular momentum $j = \Omega r^2\sin^2\theta$ is conserved along flowlines, as expected under our assumption of axisymmetry. The mass and entropy equations (1) and (3) reduce to

$$\frac{1}{r^2}\frac{\partial}{\partial r}(\rho v_r r^2) + \frac{1}{r\sin\theta}\frac{\partial}{\partial\theta}(\rho v_\theta\sin\theta) = 0, \tag{21}$$

$$v_r\frac{\partial\ln K}{\partial r} + v_\theta\frac{\partial\ln K}{r\partial\theta} = -\frac{1}{t_{\rm cool}}\,. \tag{22}$$

At large radii where the centrifugal terms in equations (18) and (19) are small, the solution will approach the spherical no-angular momentum solution discussed in Section 2.1. In this limit, we also expect $v_\theta \to 0$, so equation (20) implies that angular momentum is independent of radius, that is, it preserves the relation between j and θ that exists in the outer boundary of the flow at $r \sim r_{\rm cool}$. We denote this boundary condition as

$$j_1(r,\theta) = v_c(R_{\rm c,max})R_{\rm c,max}\sin^2\theta F(\theta)\,, \tag{23}$$

where $R_{\rm c,\,max} \equiv R_c(\theta=\pi/2)$ and thus $v_c(R_{\rm c,\,max})R_{\rm c,\,max}$ is the specific angular momentum at $\theta = \pi/2$ (see equation 13), while F is some function that satisfies $F(\pi/2) = 1$. The subscript '1' denotes that this relation is valid at large radii where $v_\theta \to 0$. Equivalently, the angular frequency at large radii is

$$\Omega_1(r,\theta) = \frac{v_c(R_{\rm c,max})R_{\rm c,max}}{r^2}F(\theta)\,. \tag{24}$$

Equation (23) implies that the circularization radius of a flowline which originates at polar angle θ is $\approx R_{\rm c,\,max}\sin^2\theta F(\theta)$, with this expression being exact for constant v_c. We show below that flowlines accrete onto the disc at a cylindrical radius equal to their circularization radius. To avoid flowline intersection, $\sin^2\theta F(\theta)$ is assumed to monotonically increase at $0 \le \theta \le \pi/2$, and thus the mid-plane flowline has the largest circularization radius.

The function F can be estimated using the results of non-radiative cosmological simulations, which provide the initial conditions (ICs) in the hot gas before a radiatively driven inflow develops. Sharma, Steinmetz & Bland-Hawthorn (2012b) found that Ω is weakly dependent on θ in a sample of $10^{11} - 10^{13}\,{\rm M}_\odot$ haloes in such simulations, with differences of ≈ 15 per cent between the mid-plane and the rotation axis. This suggests $F(\theta) \approx 1$, so we use $F(\theta) = 1$ as our fiducial value.

We note that the Sharma et al. (2012b) simulations also suggest $j \propto r^{0.5} - r^{0.7}$ at $0.1 < r/r_{\rm vir} < 1$ (see their fig. 2), that is, the initial specific angular momentum profile of the hot gas increases outwards. We thus expect this increasing j profile to be replaced by a flat $j \propto r^0$ profile (equation 23) once the inflow develops. Assuming the outer boundary of the inflow expands with time as $r_{\rm cool}$ grows (see Section 2.1), then we expect the normalization of the j profile and hence $R_{\rm c,\,max}$ to increase with time, as the inflow originates from larger radii where j is larger. This expected evolution however occurs on a cosmological timescale, and thus does not invalidate our steady-state assumption in the inner CGM which is achieved on the shorter cooling timescale at small CGM radii. Thus, for the purpose of deriving this steady-state solution in the inner CGM we treat $R_{\rm c,\,max}$ as a constant.

2.4 Analytic solution in the slow rotation limit

In this section, we derive a solution to equations (18)–(22) which is accurate to lowest order in the effects of rotation. A similar approach was employed to study meridional flows in the Sun (Sweet 1950; Tassoul 2007) and in Bondi flows with $r_{\rm sonic} \gg R_c$ (Cassen & Pettibone 1976).

The dynamical effects of rotation on hot CGM inflows increase with decreasing r, and become dominant at $r \lesssim R_{\rm c,\,max}$. To find the solution in the slow rotation limit we thus keep only terms which depend on $R_{\rm c,\,max}/r$ to the lowest order. It is straightforward to show that there are no terms of order $(r/R_{\rm c,\,max})^{-1}$, since the lowest order of Ω is proportional to $(r/R_{\rm c,\,max})^{-2}$ (equation 24) and rotation enters the other flow equations only via the term $\Omega^2 r^2$ (equations 18 and 19). We thus define a perturbation parameter

$$\epsilon = \left(\frac{r}{R_{\rm c,max}}\right)^{-2}\,, \tag{25}$$

and search for a solution of the form

$$\begin{aligned}
P_1(r,\theta) &= P_0(r)\left[1+\epsilon(r)f_P(\theta)\right],\\
\rho_1(r,\theta) &= \rho_0(r)\left[1+\epsilon(r)f_\rho(\theta)\right],\\
v_{r,1}(r,\theta) &= v_{r,0}(r)\left[1+\epsilon(r)f_{v_r}(\theta)\right],\\
v_{\theta,1}(r,\theta) &= v_{r,0}(r)\epsilon(r)f_{v_\theta}(\theta),\\
\Omega_1(r,\theta) &= \frac{v_c}{R_{\rm c,max}}\epsilon(r)\,.
\end{aligned} \tag{26}$$

Here, a subscript '0' denotes the non-rotating solution (equation 10), a subscript '1' denotes the approximate solution which we wish to find, and $f_P, f_\rho, f_{v_r}, f_{v_\theta}$ are some functions of θ. The motivation for the form of $v_{\theta,1}$ will become apparent below. The solution for Ω_1 is equivalent to equation (24) assuming $F(\theta) = 1$ as suggested by non-radiative cosmological simulations. The implications of other forms of $F(\theta)$ on the solution are discussed below.

We emphasize that the assumption of mild rotation is on top of the assumption of quasi-hydrostatic conditions, which allowed neglecting the quadratic velocity terms. Together, these assumptions imply that we assume the following conditions on timescales in the system:

$$t_{\rm sc} \approx t_{\rm ff},\quad t_{\rm cool} \gg t_{\rm ff},\quad t_{\rm rot}^2 \gg t_{\rm ff}^2\,, \tag{27}$$

where $t_{\rm sc}$ is the sound crossing time which is approximately equal to $t_{\rm ff}$ since the flow is quasi-hydrostatic, and $t_{\rm rot} = \Omega^{-1}$ is the rotation time. The squares on the relation between $t_{\rm rot}$ and $t_{\rm ff}$ follow from the relative size of the neglected centrifugal terms, which are of order $(\Omega r/v_c)^2 \sim (t_{\rm rot}/t_{\rm ff})^{-2}$ (equations 18 and 19).

Using equation (26) in equation (19), and keeping only first-order terms in ϵ, we get

$$P_0\frac{{\rm d}f_P}{{\rm d}\theta} = \rho_0 v_c^2\sin\theta\cos\theta\,, \tag{28}$$

where P_0 can be derived from $P = (3/5)\rho c_s^2$ and equation (10):

$$P_0 = \frac{2}{3}\rho_0 v_c^2 \,. \tag{29}$$

We thus get

$$f_P = \frac{3}{4}\sin^2\theta + \mathcal{C} \,, \tag{30}$$

where $\mathcal{C}$ is a constant of integration to be determined below. Next, the first-order terms in equation (18) give

$$f_P P_0 \frac{\mathrm{d}(\ln\epsilon)}{\mathrm{d}r} + f_P \frac{\mathrm{d}P_0}{\mathrm{d}r} = -f_\rho \rho_0 \frac{v_c^2}{r} + \rho_0 \frac{v_c^2}{r}\sin^2\theta \,. \tag{31}$$

Using equations (10), (25), and (29) then gives

$$f_\rho = \frac{11}{4}\sin^2\theta + \frac{7}{3}\mathcal{C} \,. \tag{32}$$

We can also define $T_1 = T_0(1 + \epsilon f_T)$. Since $T \propto P/\rho$, we get to first order in ϵ that

$$f_T = f_P - f_\rho = -2\sin^2\theta - \frac{4}{3}\mathcal{C} \,, \tag{33}$$

and similarly defining $K_1 = K_0(1 + \epsilon f_K)$ and using $K \propto P/\rho^{5/3}$, we get

$$f_K = f_P - \frac{5}{3}f_\rho = -\frac{23}{6}\sin^2\theta - \frac{26}{9}\mathcal{C} \,. \tag{34}$$

Equations (30), (32), and (33) indicate that the pressure and density increase when traversing from the rotating axis to the mid-plane at a fixed r, while the temperature decreases. The increase in pressure in the mid-plane is due to the higher density, which overcomes the lower effective gravity in the mid-plane which tends to decrease the pressure.

In the entropy equation (22), the second term on the left-hand side is of order ϵ^2 (see equation 26) and can be neglected. The first-order terms of this equation are hence

$$v_{r,0} f_K \frac{\partial \ln\epsilon}{\partial r} + v_{r,0} f_{v_r} \frac{\partial \ln K_0}{\partial r} = -\frac{1}{t_{\mathrm{cool},0}}\left[f_\rho - (1+l) f_T\right] , \tag{35}$$

where we use $t_{\mathrm{cool}} \propto T/\rho\Lambda$, and approximate the temperature dependence of the cooling function as a power-law $\Lambda = \Lambda(T_0, Z)(T/T_0)^{-l}$. Further using $K_0 \propto T_0/\rho_0^{2/3} \propto r$ and $t_{\mathrm{cool},0} = -r/v_{r,0}$ based on equation (10), and the above relations for f_K, f_ρ, f_T, we get

$$f_{v_r} = \left(-\frac{35}{12} + 2l\right)\sin^2\theta - \left(-\frac{19}{9} + \frac{4}{3}l\right)\mathcal{C} \approx -\frac{23}{12}\sin^2\theta - \frac{13}{9}\mathcal{C} \,. \tag{36}$$

In the approximation on the right we use $l = 0.5$, appropriate for gas with $T \sim 10^6$ K and a characteristic CGM metallicity of $Z \approx 0.3\,Z_\odot$ (Miller & Bregman 2015). Last, we use the continuity equation (21) to derive v_θ, which we cast in the form $v_{\theta,1} = v_{r,0}\epsilon f_{v_\theta}$ (see equation 26). Keeping only first-order terms, we get

$$\frac{\rho_0 \epsilon v_{r,0}}{r\sin\theta}\frac{\partial}{\partial\theta}\left(f_{v_\theta}\sin\theta\right) = -\frac{f_\rho + f_{v_r}}{r^2}\frac{\partial}{\partial r}\left(\epsilon\rho_0 v_{r,0} r^2\right) \,. \tag{37}$$

Using the definition of ϵ and that $\rho_0 v_{r,0} r^2$ is independent of r, we then get

$$\frac{\partial}{\partial\theta}\left(\sin\theta\, f_{v_\theta}\right) = 2\sin\theta(f_\rho + f_{v_r}), \tag{38}$$

so

$$\begin{aligned} f_{v_\theta} &= \frac{1}{\sin\theta}\int\left(\frac{5}{3}\sin^3\theta + \frac{16}{9}\mathcal{C}\sin\theta\right)\mathrm{d}\theta \\ &= \frac{1}{9\sin\theta}\left[\cos\theta\left(5\cos^2\theta - 15 - 16\mathcal{C}\right) + \mathcal{D}\right] \,, \end{aligned} \tag{39}$$

where $\mathcal{D}$ is another constant of integration. We further require $v_\theta(\pi/2) = v_\theta(0) = 0$, in order to avoid a discontinuity at the rotation axis and to enforce symmetry with respect to the mid-plane. This gives $\mathcal{D} = 0$ and $\mathcal{C} = -5/8$, and hence

$$f_{v_\theta} = -\frac{5}{18}\sin 2\theta \,. \tag{40}$$

Note that since $v_{r,0}$ is negative, then $v_{\theta,1} = v_{r,0} f_{v_\theta}\epsilon$ is positive for $\theta < \pi/2$ and negative for $\theta > \pi/2$, indicating that rotation diverts the flow towards the disc plane, as expected.

To summarize our solution we use the derived $\mathcal{C} = -5/8$ in equations (30), (32), (33), and (36) and get

$$\begin{aligned} P_1 &= P_0(r)\left(1 + \frac{R_{\mathrm{c,max}}^2}{r^2}\left(\frac{3}{4}\sin^2\theta - \frac{5}{8}\right)\right) , \\ \rho_1 &= \rho_0(r)\left(1 + \frac{R_{\mathrm{c,max}}^2}{r^2}\left(\frac{11}{4}\sin^2\theta - \frac{35}{24}\right)\right) , \\ T_1 &= T_0\left(1 - \frac{R_{\mathrm{c,max}}^2}{r^2}\left(2\sin^2\theta - \frac{5}{6}\right)\right) , \\ v_{r,1} &= v_{r,0}(r)\left(1 - \frac{R_{\mathrm{c,max}}^2}{r^2}\left(\frac{23}{12}\sin^2\theta - \frac{65}{72}\right)\right) , \\ v_{\theta,1} &= -v_{r,0}(r)\cdot\frac{5}{18}\frac{R_{\mathrm{c,max}}^2}{r^2}\sin(2\theta), \\ \Omega_1 &= \frac{v_c R_{\mathrm{c,max}}}{r^2} , \end{aligned} \tag{41}$$

where the zero-order terms are given by equation (10). For a given v_c, the solution in equation (41) depends on three parameters: $\dot{M}$ and $\Lambda(T_0, Z)$ (or equivalently CGM mass and metallicity) which set the non-rotating solution, and $R_{\mathrm{c,\,max}}$ which sets the corrections due to rotation.

The solution in equation (41) is for an outer boundary condition in which Ω_1 is independent of θ (i.e. $F(\theta) = 1$). In Appendix A, we give several solutions for $\Omega_1(\theta) \propto \sin^n(\theta)$ with integer n, that is, the rotation frequency at the outer boundary increases with angle from the rotation axis. In these solutions, the θ-dependent term in the solution for P_1 is multiplied by a factor of $\sin^{2n}(\theta)/(n+1)$ relative to that in equation (41), while the corresponding term for T_1 is multiplied by a factor of $\sin^{2n}(\theta)\cdot(n+2)/(n+1)$. Thus, the result above that P and ρ increase towards the mid-plane, while T decreases, holds also when Ω_1 increases with θ. These deviations from spherical symmetry however tend to become weaker, and more concentrated near the mid-plane, with increasing n.

2.5 Number of revolutions in CGM inflows

The number of revolutions around the rotation axis completed by a flowline can be derived from the ratio v_ϕ/v_r implied by equation (41):

$$\frac{v_\phi}{v_r} = \frac{\Omega r\sin\theta}{v_r} = \frac{v_c R_{\mathrm{c,max}}\sin\theta}{r v_{r,0}}\left(1 + \mathcal{O}(\epsilon)\right) \,. \tag{42}$$

Using $v_{r,0} = r/t_{\mathrm{cool}}(1 + \mathcal{O}(\epsilon))$ and $t_{\mathrm{ff}} = \sqrt{2}r/v_c$, we thus get

$$\frac{v_\phi}{v_r} = \sqrt{2}\frac{t_{\mathrm{cool}}}{t_{\mathrm{ff}}}\frac{R_{\mathrm{c,max}}}{r}\sin\theta\left(1 + \mathcal{O}(\epsilon)\right) \,. \tag{43}$$

It is thus evident that in solutions with larger $t_{\mathrm{cool}}/t_{\mathrm{ff}}$ the flowlines are more tightly wound, that is, the flow rotates more prior to accreting onto the galaxy. The total number of radians a flowline rotates can

be approximated with the following integral

$$\int \Omega \mathrm{d}t = \int \frac{v_\phi}{r \sin\theta} \frac{\mathrm{d}r}{v_r} \approx \sqrt{2} \int \frac{t_{\rm cool}}{t_{\rm ff}} \frac{R_{\rm c,max}}{r^2} dr \approx 2 \frac{t_{\rm cool}}{t_{\rm ff}}(R_{\rm c,max}) \,, \tag{44}$$

where in the first approximation we used equation (43) and in the second approximation we used $t_{\rm cool}/t_{\rm ff} \propto r^{1/2}$ (equation 10) and integrated over the range $r/R_{\rm c,\,max} = 1$–7. The upper bound of this range corresponds to the cooling radius (see Section 2.1), though since the integrand scales as $r^{-3/2}$ most of the rotation happens near $R_{\rm c,\,max}$, and the choice of upper limit does not significantly affect the result. Also, the lower bound of this range implies that neglecting the $O(\epsilon)$ term is not formally justified. Below we validate this approximation with a more accurate numerical calculation. Equation (44) suggests that the number of rotations is set by $t_{\rm cool}/t_{\rm ff}$ near $R_{\rm c,\,max}$, where $t_{\rm cool}/t_{\rm ff}$ is estimated by the non-rotating solution (equation 10). This can be understood intuitively since the cooling time tracks the inflow time ($t_{\rm cool} = r/|v_r|$) while the free-fall time tracks the rotation time near $R_{\rm c,\,max}$ ($t_{\rm ff} \approx r/v_{\rm c} = r/v_\phi(R_{\rm c,\,max})$). For the Milky Way halo in which $t_{\rm cool}/t_{\rm ff}(R_{\rm c,\,max}) \approx 6$ (equation 16), we get that an accreting element rotates $\approx$12 radians prior to accretion. Furthermore, since $t_{\rm cool}/t_{\rm ff}$ increases with $v_{\rm c}$ (see equation 10), we generally expect the amount of rotation to increase with galaxy mass.

It is informative to extend the result in equation (44) also to galaxies with halo masses $\ll 10^{12}\,\mathrm{M}_\odot$, where $t_{\rm cool} < t_{\rm ff}$ and the volume-filling phase is cool and in free-fall with $v_r \approx -v_{\rm c}$ (e.g. Stern et al. 2020). Using $-v_r = \min(r/t_{\rm cool}, v_{\rm c})$ in equation (44) we thus get

$$\int \Omega \mathrm{d}t \approx \max(2 \frac{t_{\rm cool}}{t_{\rm ff}}(R_{\rm c,max}), 1). \tag{45}$$

Equation (45) demonstrates that only in the hot accretion mode where pressure-support slows down accretion relative to free-fall, the CGM has time to rotate significantly before accreting. In contrast, free-falling cold flows rotate merely by $\approx$1 radian prior to accretion.

The ratio $t_{\rm cool}/t_{\rm ff}$ at $r = R_{\rm c,\,max}$ fully determines the hot rotating inflow solution, up to a scaling of the physical dimensions, as we show in Appendix B using non-dimensional analysis of the flow equations. We similarly show that the solution is fully determined up to a scaling by the ratio $\dot{M}/\dot{M}_{\rm crit}$, where $\dot{M}_{\rm crit}$ is the critical accretion rate in which $t_{\rm cool}/t_{\rm ff} = 1$ at $r = R_{\rm c,\,max}$ (Stern et al. 2020).

2.6 Disc accretion radius

The distribution of disc radii at which gas accretes is an important input parameter for chemical evolution models and dynamical models of galaxy discs (e.g. Schönrich & Binney 2009; Krumholz et al. 2018; Wang & Lilly 2022). In this section, we derive this distribution for hot and rotating CGM inflows.

Since the flow is spherical at large radii it holds that

$$\frac{\mathrm{d}\dot{M}}{\mathrm{d}\theta_0} = \frac{1}{2}\dot{M} \sin\theta_0 \,, \tag{46}$$

where we use θ_0 to denote the polar angle of a flowline at large radii. In hot rotating CGM inflows flowlines both conserve angular momentum (equation 20), and accrete onto the disc at their circularization radius $R_{\rm c}(\theta_0)$ (see numerical calculation below). The value of $R_{\rm c}$ can be estimated from equation (23), which for constant $v_{\rm c}$ and $F(\theta_0) = 1$ implies

$$R_{\rm c}(\theta_0) = R_{\rm c,max} \sin^2\theta_0 \,. \tag{47}$$

We thus get

$$\dot{M}_{\rm disc}(<R) = 2\int_0^{\theta_0(R)} \frac{\mathrm{d}\dot{M}}{\mathrm{d}\theta_0'} d\theta_0' = \dot{M}(1-\cos\theta_0) = \left\{ \begin{array}{ll} \dot{M}\left(1-\sqrt{1-R/R_{\rm c,max}}\right) & R \le R_{\rm c,max} \\ \dot{M} & R \ge R_{\rm c,max} \end{array} \right\} , \tag{48}$$

where the factor of 2 before the integral accounts for the two sides of the disc. Equation (48) indicates that the median accretion radius is $(3/4)R_{\rm c,\,max}$, or 11.25 kpc for $R_{\rm c,max} = 15$ kpc, suggesting accretion weighted towards large disc radii. A similar conclusion of accretion mainly from large disc radii was deduced in FIRE cosmological simulations of Milky Way-like galaxies, in which the accretion is also dominated by hot rotating inflows (Trapp et al. 2022).

3 THE STRUCTURE OF HOT AND ROTATING CGM – NUMERICAL SOLUTION

In this section, we derive numerical solutions for hot and rotating CGM inflows. To this end, we run 3D hydrodynamic simulations until they converge onto a steady state, where mass continuously flows through the hot CGM, cools and accretes onto the disc, and forms stars. Using this method to find the numerical solution has the advantage that it demonstrates that the solution is an attractor. The properties of the numerical solution are then compared to the approximate analytic solution derived in the previous section.

3.1 Setup

We use the meshless finite-mass ('MFM') mode of GIZMO (Hopkins 2015), a Lagrangian method with no inter-element mass flux, which enables us to track the history of each resolution element. The code accounts for self-gravity of the gas and stars, to which we add an acceleration term $-(v_{\rm c}^2/r)\hat{r}$ with $v_{\rm c} = 200\,\mathrm{km\ s^{-1}}$. This term approximates the gravitational field in the inner halo due to unmodelled dark matter and stars. Optically thin radiative cooling is calculated using the $z = 0$ tables from Wiersma, Schaye & Smith (2009) down to $T = 10^4$ K, while optically thick radiative cooling to lower temperatures is disabled. All gas resolution elements with $n_{\rm SF} > 10\,\mathrm{cm^{-3}}$ are converted into stellar particles. All stellar feedback processes are disabled.

The density, temperature, and radial velocity of gas is initialized with a spherical, non-rotating hot inflow solution from Stern et al. (2019), to which we add rotation corresponding to some $R_{\rm c,\,max}$. This solution is found by integrating the 1D spherically symmetric and steady-state flow equations, starting at $r_{\rm sonic} = 0.1$ kpc and proceeding outward. The integration uses the same $v_{\rm c} = 200\,\mathrm{km\ s^{-1}}$ and cooling function with $Z = 0.3\,\mathrm{Z}_\odot$ as in the simulation. The 1D solution has $\dot{M} = 1\,\mathrm{M}_\odot\,\mathrm{yr}^{-1}$ and at radii $r \gg r_{\rm sonic}$ is well approximated by equation (10), with $T = 2\times10^6$ K and $\Lambda_{-22} = 0.3$. We then randomly select initial positions in (r, ϕ, θ) for the initial location of gas resolution elements, such that the radial mass profile reproduces that in the spherically symmetric solution. To add a net rotation to the gas, all resolution elements at $r > R_{\rm c,\,max}$ are initialized with $v_\phi = 200\sin\theta(r/R_{\rm c,max})^{-1}\,\mathrm{km\ s^{-1}}$, with $R_{\rm c,max} = 15$ kpc. This addition of rotation implies that the ICs are not in steady state, since the initial pressure structure does not account for rotation support. We show below that the simulation adjusts to a new steady state within a cooling time of < 1 Gyr, with a somewhat larger $\dot{M}$ of $1.7\,\mathrm{M}_\odot\,\mathrm{yr}^{-1}$.

The mass of individual resolution elements is set to $m_b = 1000\,\mathrm{M}_\odot$ for elements at $r < 100$ kpc. This mass resolution implies a characteristic size of $\approx (3m_b/4\pi n_{\rm H})^{1/3} \approx 0.2 n_{-3}^{-1/3}$ kpc for typical hot gas

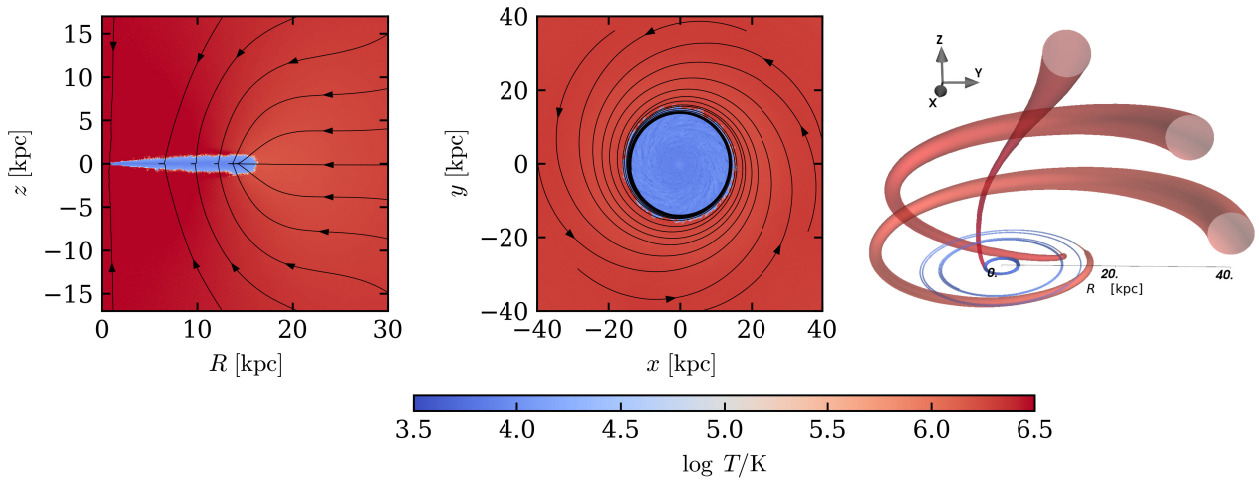

Figure 1. Temperature map (colour) and flowlines (black lines) in a hot rotating CGM inflow. Left and middle panels show the solution in the cylindrical $R - z$ and the $x - y$ planes. The right panel depicts three specific flowlines as 3D 'tubes', where the cross-section along each tube scales as $(\rho v)^{-1}$ and hence illustrates the compression of the flow. Note that the hot $\sim 10^6$ K phase inflows along helical paths, and cools to $\sim 10^4$ K just prior to joining the ISM disc.

densities of $\approx 10^{-3} n_{-3}\,\mathrm{cm}^{-3}$ near the disc scale, and smaller sizes for the denser cool gas. For comparison, the height of the $\approx 10^4$ K gaseous disc which forms from the cooling of the hot gas is ≈ 1 kpc.[2]

Beyond 100 kpc, the gas does not participate in the inflow since cooling times are too long, but needs to be included in the simulation in order to confine gas at smaller radii from expanding outward (in a realistic halo this confinement is achieved either by such hot gas with a long cooling time or by the ram pressure of infalling gas outside the accretion shock). To avoid investing too much computing time in this confining outer gas, we sample the spherically symmetric solution beyond 100 kpc with resolution elements which masses increase by a factor of three every factor of $\sqrt{2}$ in radius, out to 3.2 Mpc where the sound-crossing time equals 10 Gyr. In total, the CGM is simulated with 3.1×10^7 resolution elements.

We also add a galaxy to the ICs, using the MAKEDISK code (Springel, di Matteo & Hernquist 2005) with the following parameters. The stellar disc is initialized with mass $M_* = 10^8\,\mathrm{M}_\odot$, cylindrical radial scale length of $R_\mathrm{d} = R_\mathrm{c,max}/4 = 3.75$ kpc spanning $0.03 - 4R_\mathrm{d}$, and a vertical scale length of $0.1R_\mathrm{d}$. The gaseous disc has a mass $M_\mathrm{disc\,gas} = 0.2M_*$, and the same exponential distribution as stars, and the bulge has a mass $M_\mathrm{bulge} = 2 \times 10^7\,\mathrm{M}_\odot$ and scale length 0.1 kpc. We include in the MAKEDISK calculation the same isothermal gravitational field used in the hydro simulation, and stellar and gas particles in the disc have the same $m_b = 1000\,\mathrm{M}_\odot$ resolution as in the CGM. The choice of galaxy parameters is inconsequential as long as the initial mass is small compared to the accreted mass, which at $t = 1$ Gyr is $\dot{M}t \sim 10^9\,\mathrm{M}_\odot$. The simulation is run for 3.5 Gyr, with snapshots saved every 5 Myr. At all times and radii, the gravitational field is dominated by the included isothermal gravitational field with $v_\mathrm{c} = 200\,\mathrm{km\,s}^{-1}$, rather than by the simulated gas and stars.

Our setup is loosely based on the setup of Su et al. (2019, 2020), which simulated the behaviour of gas in group and cluster-sized haloes. A similar setup to ours for Milky Way mass haloes was employed by Kaufmann et al. (2006) using a smoothed particle hydrodynamics code. This code was later found to overpredict artificial clumping of the cool gas (Agertz et al. 2007; Kaufmann et al. 2009). Our use of the MFM code addresses this numerical issue (see Hopkins 2015, for code tests). Additionally, since in our simulation *all* the hot gas cools once it inflows past $R_\mathrm{c,\,max}$ (see below), the numerical details may affect the distribution of clumps and their typical sizes, but not the total mass which cools.

[2]This follows since the disc height to radius ratio is $\approx c_\mathrm{s}/v_\mathrm{c}$, and hence for a gaseous disc temperature 10^4 K we get $(c_\mathrm{s}/v_\mathrm{c})R_\mathrm{c,max} \approx 1$ kpc.

3.2 Overview of results

Fig. 1 shows temperature maps in the simulation at $t > 1$ Gyr, after the hot CGM phase converged onto an axisymmetric steady-state solution within $r \approx 40$ kpc. Steady state and axisymmetry are evident from the small dispersion in hot CGM properties with time and ϕ, as shown below. The left and middle panels, respectively, show the $R - z$ and the $x - y$ planes (mass-weighted over $-10 < z < 10$ kpc). The figure shows that the hot gas fills the volume except in the disc region at $R \lesssim R_\mathrm{c,max} = 15$ kpc and $|z| \lesssim 1$ kpc. Black lines depict flowlines in the two planes, derived as described below. Three of these flowlines are also depicted in the right panel as 3D 'tubes', rendered using the MAYAVI software (Ramachandran & Varoquaux 2011) on snapshot data. The tube cross-section scales as $(\rho v)^{-1}$ and thus illustrates the compression of the flow.

Fig. 1 shows that the flowlines in the hot gas are helical, with the hot gas spiraling onto the galaxy. While inflowing, the gas initially remains hot with $T \sim T_\mathrm{vir}$, and then cools to $\sim 10^4$ K just prior to joining the ISM disc. This cooling is accompanied with strong compression of the flow, as evident from the sharp decrease in the width of the flow tubes in the right panel (tube thickness should drop to $\lesssim 0.01$ pixels upon cooling according to the $(\rho v)^{-1}$ scaling, though is plotted with one pixel for visibility).

Fig. 2 plots radial shell-averaged velocities in the simulation after steady state is achieved. The top panel shows that at radii $r > R_\mathrm{c,\,max}$ the sound speed c_s (red) approximately equals v_c (grey), indicating the hot gas is to first order supported against gravity by thermal pressure, as indicated also by the slow inflow velocities of $-v_r \ll v_\mathrm{c}$ (magenta line). At radii $r > R_\mathrm{c,\,max}$, the rotation velocity increases inward roughly as r^{-1} due to conservation of angular momentum, reaching $v_\phi = v_\mathrm{c}$ at $R_\mathrm{c,\,max}$. Within $R_\mathrm{c,\,max}$ the gas is fully rotationally supported and cool with $c_s \ll v_\mathrm{c}$, and the radial velocity drops to zero.

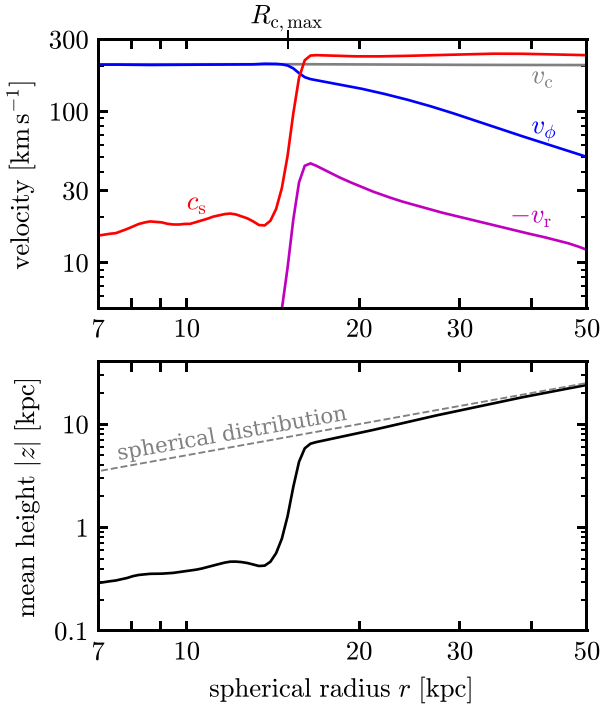

Figure 2. Radially averaged kinematics and geometry of a hot rotating CGM inflow. Top: lines show sound speed (red), rotation velocity (blue), and inflow velocity (magenta). Bottom: black line shows the average absolute height above the mid-plane. Rotation velocity increases inward due to conservation of angular momentum. At radii $r < R_{\rm c,\,max}$, where the inflow becomes fully rotation supported ($v_\phi = v_{\rm c}$) the hot inflow cools out, the inflow halts ($|v_r| \rightarrow 0$), and the geometry transitions from quasi-spherical to a disc.

The associated change in geometry is evident in the bottom panel, which plots the average absolute height above the mid-plane $|z|$ in different radial shells. The gas distribution is close to spherically symmetric at $r > R_{\rm c,\,max}$, in contrast with a thin disc distribution at $r < R_{\rm c,\,max}$.

3.3 Accretion of the hot CGM onto the cool ISM

Fig. 3 provides a Lagrangian view of hot inflowing CGM, by plotting median properties of resolution elements versus time since the element was at $r = 40$ kpc. The properties depend on the initial polar angle of the flowline θ_0, so for each θ_0 in $(0.1\pi, 0.3\pi, 0.4\pi, 0.5\pi)$ we group all resolution elements that reside at $40 < r < 41$ kpc and $|\theta - \theta_0| < 0.025\pi$ at times $1 < t < 1.5$ Gyr. Then, for each θ_0 group we plot the median and 16–84 percentile ranges of r, θ, T, and v_ϕ. The 16–84 percentile range thus accounts for the dispersion both with ϕ and with t, and specifically a small 16–84 percentile range indicates that the solution is axisymmetric and in steady state.

Fig. 3 shows that at $r \gtrsim 25$ kpc (early times in this plot), the gas is hot and inflowing, with a somewhat larger inflow velocity in the $\theta_0 = 0.1\pi$ flowline near the rotation axis. Rotation is sub-Keplerian ($v_\phi < v_{\rm c} \approx 200\,{\rm km\,s^{-1}}$) but growing with time, as also indicated by Fig. 2. The value of θ remains roughly constant and equal to θ_0 for a given flowline. Then, when the flowlines reach radii of $r \lesssim 20$ kpc, the gas initially heats up and is diverted to the mid-plane ($\theta = \pi/2$), and then abruptly cools. The initial heating is more pronounced near the rotation axis, and is a result of the compression due to the change in geometry from spherical to disc-like (see below). Cooling occurs simultaneously with θ reaching $\pi/2$, v_ϕ reaching $v_{\rm c} \approx 200\,{\rm km\,s^{-1}}$,

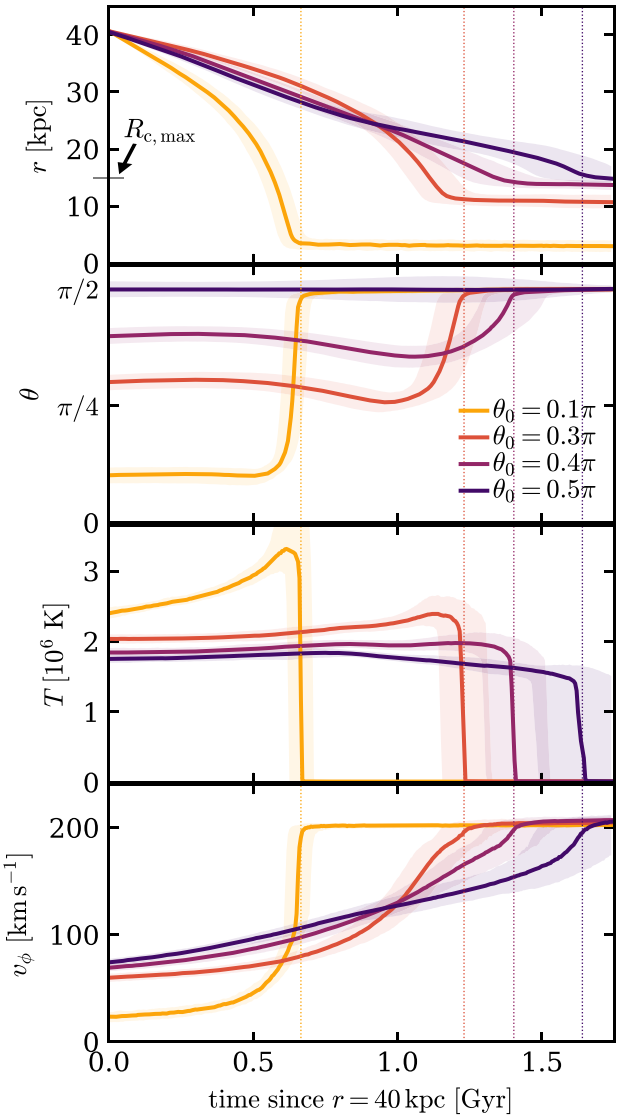

Figure 3. Gas properties along flowlines in hot rotating CGM inflows, versus time since a fluid element is at $r = 40$ kpc. Panels show spherical radius, polar angle, temperature, and rotation velocity. Different lines and bands correspond to medians and 16th–84th percentiles of flowlines with different polar angles at large radii θ_0. Vertical dotted lines indicate times where T drops to 10^5 K. Initially the flowlines have roughly constant $\theta \approx \theta_0$. About 200 Myr prior to cooling the flow geometry flattens ($\theta \rightarrow \pi/2$), and the temperature increases mainly in flowlines with small θ_0. Cooling occurs when v_ϕ reaches $v_{\rm c} \approx 200\,{\rm km\,s^{-1}}$, that is, at the circularization radius of the flowline $R_{\rm c}(\theta_0)$, indicating a transition from quasi-thermal pressure support against gravity to rotational support. Dispersion in hot gas properties prior to cooling is small, demonstrating the hot inflow is steady and axisymmetric.

and r becoming constant, that is, when the hot gas has achieved full rotational support and transitioned to a flat, disc geometry. We thus identify the time of cooling also as the time of accretion from the hot CGM onto the ISM. A similar relation between cooling and accretion was identified by Hafen et al. (2022) in cosmological zoom simulations of $z \sim 0$ Milky Way-mass galaxies from the FIRE project.

Note also that prior to cooling the 16–84 percentile ranges in individual flowlines are small, indicating the hot CGM is axisymmetric and in steady state. Furthermore, cooling and accretion happens to all hot inflow resolution elements, indicating that cooling is a global

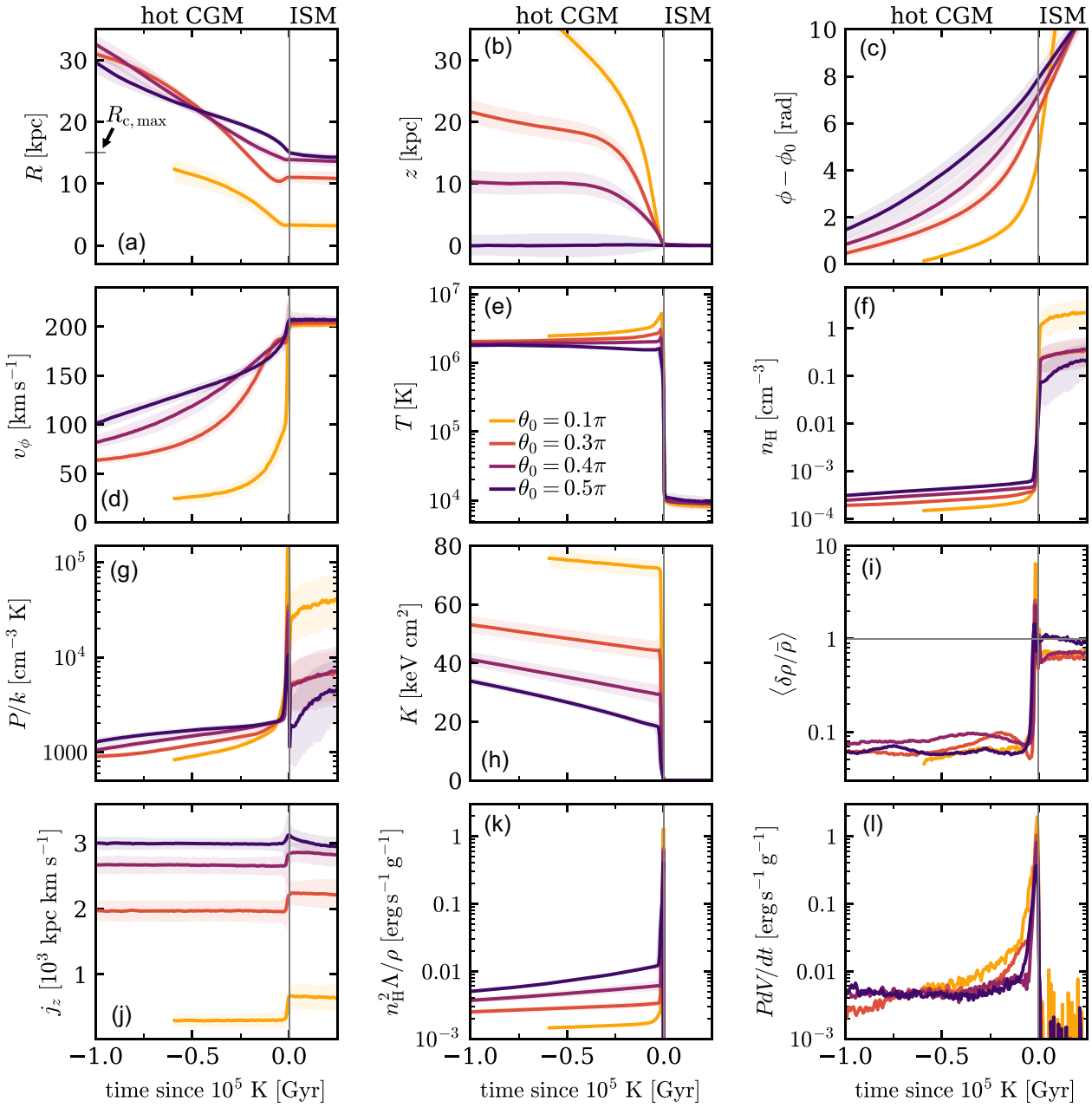

Figure 4. Gas properties along flowlines in hot rotating CGM inflows, versus time since gas in the flowline cools. The time of cooling is equal to the time of accretion onto the ISM. From left to right and top to bottom the panels plot cylindrical radius, height above the mid-plane, total rotation since $r = 40$ kpc, rotational velocity, density, temperature, pressure, entropy, density dispersion, specific angular momentum, radiative losses per unit mass, and compressive heating rate per unit mass. Coloured lines and bands correspond to medians and 16th–84th percentile ranges of flowlines with different polar angles at large radii θ_0, except in panel l, where lines denote mean values. At early times $t - t(10^5\,{\rm K}) < -200$ Myr, the temperature remains roughly constant at $\approx 2 \times 10^6$ K (panel e) since compressive heating and radiative cooling roughly balance (panels k–l). Also, density fluctuations are small (panel i), and the specific angular momentum is conserved (panel j). About 200 Myr prior to cooling the geometry of the flow starts to flatten into a disc (panel b). At $t \approx t(10^5\,{\rm K})$ rotation velocity reaches the circular velocity (panel d), densities increase by $\times$ 300 or more (panel f), and density fluctuations become significant (panel i).

transition in the inflow, rather than occuring only in individual gas clumps as in precipitation models (e.g. Maller & Bullock 2004; Voit et al. 2017).

Fig. 4 plots gas properties along flowlines versus $t - t(10^5\,{\rm K})$, where $t(10^5\,{\rm K})$ is defined as the time at which the temperature in the flowline equals 10^5 K. This time is also marked with vertical lines in Fig. 3, and as mentioned above is equivalent to the time of accretion onto the ISM. The 12 panels show cylindrical radius R, z, total rotation $\phi - \phi_0$ where $\phi_0 \equiv \phi(r = 40\,{\rm kpc})$, rotation velocity, density, temperature, pressure, entropy, density dispersion, specific angular momentum, radiative cooling rate per unit mass $n_{\rm H}^2\Lambda/\rho$, and compressive heating rate per unit mass $P{\rm d}V/{\rm d}t$, where $V = \rho^{-1}$ is the specific volume. The figure shows that while the flow is hot (at $t < t(10^5\,{\rm K})$), the density and pressure of the hot

inflow mildly increase with time, while the temperature is roughly constant and the entropy decreases. The increase in density is due to the contraction of the inflow, which also causes a compressive heating ate of order $P\mathrm{d}V/\mathrm{d}t \approx 0.005\,\mathrm{erg\,s^{-1}\,g^{-1}}$. This compressive heating offsets comparable radiative losses (compare panels k and l), thus keeping the temperature roughly constant while the entropy decreases. Also, panel (i) shows that density fluctuations are small ($\langle\delta\rho/\bar{\rho}\rangle \ll 1$) as in a non-rotating cooling flow (Balbus & Soker 1989; Stern et al. 2019), and panel (j) shows that the specific angular momentum is conserved since the system is axisymmetric. Panel (c) shows that flowlines rotate 4–8 radians prior to cooling, or roughly one full revolution.

Fig. 4(f) shows that at $t \approx t(10^5\,\mathrm{K})$ when the flow abruptly cools, the density increases by a factor of ≈300 for the flowline in the mid-plane ($\theta_0 = 0.5\pi$), and by a larger factor in flowlines with smaller θ_0. At the same time j_z slightly increases (panel j), likely as a result of torques by stars and preexisting disc gas. Also apparent is that density fluctuations become strong just before the gas cools (at $t - t(10^5\,\mathrm{K}) \approx -25\,\mathrm{Myr}$), and remain of order unity after cooling, in contrast with the weak density fluctuations when the flow is hot (panel i). The transition to a disc geometry starts somewhat earlier, at $t - t(10^5\,\mathrm{K}) \approx -250$ Myr (panel b, and also θ panel in Fig. 3).

The eventual drop in temperature from $T \approx 2\times10^6$ to $\approx 10^4$ K at $t(10^5\,\mathrm{K})$ is an inevitable result of the inflow halting due to rotation support, which stops compressive heating. Absent any heating sources, the gas cools on a cooling timescale, which is ~ 10 Myr at $t(10^5\,\mathrm{K})$. This short cooling timescale is a result of the flattening to a disc geometry which increases the density to $n_\mathrm{H} \gtrsim 0.01\,\mathrm{cm^{-3}}$ [see zoom-in on $t \approx t(10^5\,\mathrm{K})$ in Fig. C1]. This layer where the hot inflow cools corresponds to the disc–halo interface (e.g. Fraternali & Binney 2008; Marasco, Fraternali & Binney 2012; Fraternali 2017), also known as 'extraplanar gas', which is further addressed in the discussion.

The result that density fluctuations remain small when the flow is hot (Fig. 4i) is potentially due to the accretion process occurring on a timescale comparable or shorter than t_cool on which thermal perturbations develop. For example, at 0.5 Gyr prior to accretion (i.e. at $t - t(10^5\,\mathrm{K}) = -0.5$ Gyr) we find $t_\mathrm{cool} = 1.7$, 2.9, 5.3, and 12 Gyr in the four flowlines shown in Fig. 4, with longer t_cool closer to the rotation axis due to the higher temperature and lower densities. The 0.5 Gyr remaining until accretion is thus insufficient for the thermal instability to grow, despite that the hot gas is formally unstable. A similar argument explains why significant density perturbations do not develop spontaneously in non-rotating cooling flows (Balbus & Soker 1989). This conclusion is also consistent with the simulations in Sormani & Sobacchi (2019), which found that condensations develop only when a heating term is added to part of the hot gas, thus increasing the accretion time relative to a cooling flow.

3.4 Deviations from spherical symmetry in hot inflowing CGM

Rotational support in the hot CGM is expected to induce lower gas densities and higher gas temperatures along the rotation axis relative to the mid-plane (Barnabè et al. 2006; Pezzulli et al. 2017; Sormani & Sobacchi 2019). In this section, we quantify these deviations from spherical symmetry in our simulation of a hot rotating inflow, and compare it to the analytic approximation deduced above (equation 41).

Fig. 5 plots the dependence of hot CGM properties on polar angle θ at radii of 45 and 25 kpc. From top to bottom the different rows plot angular frequency, temperature, hydrogen density, and thermal pressure. Magenta lines denote the non-rotating analytic solution

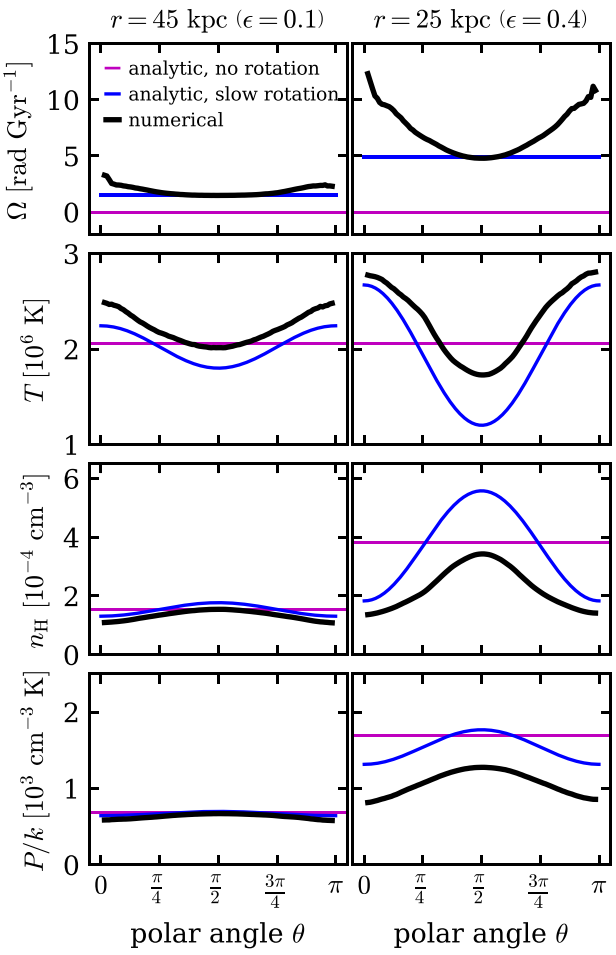

Figure 5. Deviations from spherical symmetry in hot rotating CGM inflows. Panels show from top to bottom the hot gas angular frequency, temperature, hydrogen density, and pressure, versus angle from the rotation axis θ, at $r = 45$ kpc (left) and $r = 25$ kpc (right). Black lines are based on the simulation after steady state is achieved (the same simulation as in Figs 1–4). Magenta lines plot the analytic non-rotating solution (equation 10), while blue lines plot the analytic slow-rotating solution (equation 41) which accounts only for lowest order terms in $\epsilon = (r/R_{\mathrm{c,\,max}})^{-2}$ (noted on top). In the rotating solutions density and pressure increase towards the mid-plane, while temperature decreases.

(equation 10), blue lines denote the slow rotating analytic solution (equation 41), and black lines the solution in the simulation after steady state is achieved (the same solution used in Figs 1–4). The perturbation parameter $\epsilon = (r/R_{\mathrm{c,\,max}})^{-2}$ defined in equation (25) is noted at the top. The slow-rotating analytic solution accounts only for the lowest order terms in this quantity.

Fig. 5 demonstrates how the properties of the hot gas deviate from spherical symmetry due to the rotation, and more so at radii approaching $R_{\mathrm{c,\,max}}$ where rotation support is more significant. At $r = 25$ kpc in the numerical solution, the temperature at the rotating axis is almost a factor of two lower than in the mid-plane, while the density is a factor of two higher. Note also that the slow-rotating analytic solution rather accurately reproduces the simulation at $r = 45$ kpc where $\epsilon = 0.1$. At $r = 25$ kpc, where $\epsilon = 0.4$ the analytic solution is qualitatively consistent with the trends of T, n_H, and P versus θ, though there are quantitative differences potentially since high-order terms in ϵ are neglected in the analytic solution.

Table 1. Parameters of simulations used in Fig. 6.

v_c [km s^{-1}]	$R_{c,\,max}$ [kpc]	$\dot{M}$ [M$_\odot$ yr^{-1}]	Z_{CGM} [Z$_\odot$]	t_{cool}/t_{ff} at $r = R_{c,\,max}$ [(a)]
200[(b)]	15	1.7	0.3	9.3
200	15	3.2	0.3	6.5
200	10	2.7	0.1	8.5
200	10	8.3	0.1	4.9
200	1	1.8	0.1	3.3
200	1	4.2	3.0	0.5
200	1	5.4	20	0.2
230	18	2.9	0.3	12.2
210	18	3.5	0.3	8.1
150	10	1.3	0.3	3.6
150	10	2.7	0.3	2.5
150	10	8.8	0.3	1.4
100	5	0.2	0.3	2.4
100	5	0.8	0.3	1.3

Notes.[(a)] Derived from the four other parameters using equation (10).
[(b)] Fiducial simulation used also in other figures.

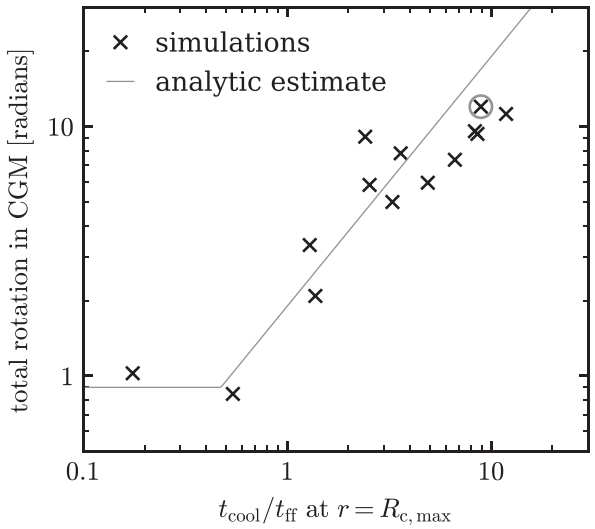

Figure 6. Total rotation completed by a fluid element in the CGM prior to accreting onto the ISM. Markers denote mean values in simulations with different t_{cool}/t_{ff} (measured at $r = R_{c,\,max}$, see Table 1), while the thin line denotes the analytic estimate from equation (45). The fiducial simulation shown in Figs 1–5 is marked with a circle. Hot CGM with longer t_{cool} have slower inflow velocities, and hence fluid elements rotate more prior to accretion.

3.5 Revolutions in inflow versus t_{cool}/t_{ff}

To test the relation between total rotation in the inflow and t_{cool}/t_{ff} measured at $R_{c,\,max}$ (Section 2.5), we run several simulations with different combinations of $\dot{M}$, Z_{CGM}, and v_c which yield different t_{cool}/t_{ff} via equation (10). The parameters of the simulations are listed in Table 1. For $\dot{M}$, we use the value measured through a shell at $2R_{c,\,max}$ in snapshots after the simulations achieve steady state, which is typically 10 per cent − 75 per cent larger than $\dot{M}$ in the ICs (see Section 3.1). On these snapshots we also measure the average rotation $\Delta\phi = \int \Omega dt$ a fluid element completes as it inflows from $10R_{c,\,max}$ to $R_{c,\,max}$, and plot them in Fig. 6. The figure shows that the simulations roughly follow the analytic estimate from equation (45), confirming that the number of rotations in hot rotating CGM scales with t_{cool}/t_{ff}.

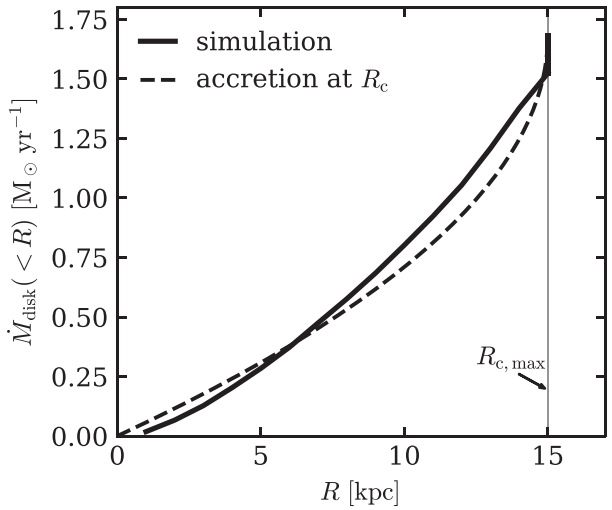

Figure 7. Accretion rate onto the disc versus disc radius in hot rotating inflows, for $R_{c,max} = 15$ kpc and total accretion rate $\dot{M} = 1.7\,M_\odot\,yr^{-1}$. The solid line is the accretion rate within a cylindrical disc radius R in the fiducial simulation. The step at $R = R_{c,\,max}$ corresponds to horizontal accretion from the disc edge. The dashed line is the analytic estimate, which assumes each flowline accretes at its circularization radius (equation 48), and provides a good match to the simulation result. This predicted $\dot{M}_{disk}$ profile in hot rotating inflows can be useful for chemical evolution models and dynamical models of galaxy discs (e.g. Schönrich & Binney 2009; Krumholz et al. 2018).

3.6 Disc accretion radius

Fig. 7 plots the accretion rate onto the disc within cylindrical disc radius R. Solid line is based on the fiducial simulation, which we measure by calculating the mass flux through two disc-shaped surfaces with radius R located at $z = \pm 1$ kpc, in a snapshot after the simulation achieved steady state. The step at $R = R_{c,max} = 15$ kpc corresponds to planar accretion from the disc edge, derived from the mass flux through a closing vertical surface spanning $-1 < z < 1$ kpc at $R = R_{c,\,max}$. The simulation result is close to the analytic estimate in equation (48), which is based on the assumption that each flowline in the hot inflow accretes at its circularization radius.

4 ADDITIONAL CONSIDERATIONS

In this section, we consider the effect of additional physical mechanisms and effects which were not included in the simulation above.

4.1 Viscosity

Viscous forces in the flow may in principle cause angular momentum transport along directions where there is shear in the flow. In our solution $\Omega \propto r^{-2}$ up to corrections of order ϵ (equation 41) and thus there is shear in the radial direction. Here, we show that for standard kinematic viscosity the expected angular momentum transport due to this shear is small.

The specific angular momentum of the flow is $j = \Omega r^2 \sin^2\theta = v_c R_{c,\,max} \sin^2\theta$ (equation 41). Viscous forces in the radial direction will cause an angular momentum loss per unit time of

$$\frac{dj}{dt} = \nu r^2 \sin^2\theta \frac{d^2\Omega}{dr^2} = 6\nu\Omega\sin^2\theta\,, \tag{49}$$

where ν is the kinematic viscosity (e.g. Fabian et al. 2005)

$$\nu = 0.56\, T_6^{5/2} \left(\frac{n_{\rm H}}{10^{-3}\,{\rm cm}^{-3}}\right)^{-1} \xi_\nu\ {\rm kpc\,km\,s^{-1}}, \tag{50}$$

and ξ_ν is the reduction of the viscosity relative to the *Spitzer* value. We can estimate the fractional angular momentum loss due to viscous forces by multiplying dj/dt by the flow time $\approx t_{\rm cool}$ and dividing by j:

$$\frac{\Delta j_{\rm visc}}{j} \approx \frac{{\rm d}j}{{\rm d}t} \cdot \frac{t_{\rm flow}}{j} = \frac{6\Omega\nu t_{\rm cool}}{v_{\rm c} R_{\rm c,max}} \approx 0.092\, \xi_\nu r_{10} v_{\rm c,200}^5 \dot{M}_1^{-1}, \tag{51}$$

where we used the analytic solution in equation (41) and neglected corrections of order $(R_{\rm c,\,max}/r)^2$. For typical estimates of $\xi_\nu \sim 0.1$ (Narayan & Medvedev 2001) this value is substantially smaller than unity, indicating that viscous forces can generally be neglected.

4.2 Turbulence

Assuming that turbulence is seeded at large CGM radii, for example by cosmological accretion or due to stirring by subhaloes, what would be the fate of these turbulent motions in the inner CGM inflow explored here? In a non-rotating inflow, we expect a balance between dissipation of turbulence on a timescale $t_{\rm diss} = r/\sigma_{\rm turb}$ and 'adiabatic heating' of turbulence due to the contraction of the inflow on a timescale $t_{\rm flow} = r/v_r$ (Robertson & Goldreich 2012). This balance suggests that contracting turbulent fluids converge to $t_{\rm flow} \sim t_{\rm diss}$ and hence $\sigma_{\rm turb} \sim v_r$, since more rapid turbulent motions will dissipate while slower turbulence will heat up (Murray & Chang 2015; Murray et al. 2017). In a steady-state cooling flow where $t_{\rm flow} \approx t_{\rm cool}$, we thus expect also $t_{\rm diss} \sim t_{\rm cool}$. Using $t_{\rm ff} \sim r/v_{\rm c}$ and $v_{\rm c} \approx c_{\rm s}$, it thus follows that

$$\frac{\sigma_{\rm turb}}{c_{\rm s}} \sim \frac{t_{\rm ff}}{t_{\rm cool}}\,. \tag{52}$$

Since $t_{\rm ff} < t_{\rm cool}$, equation (52) suggests that turbulence is subsonic, i.e. turbulent support is subdominant to thermal support, as assumed in Section 2.1. Furthermore, this relation suggests that relative importance of turbulent motions decreases with increasing $t_{\rm cool}/t_{\rm ff}$.

Note that equation (52) is based on the assumption that the dominant turbulence driving mechanism at inner CGM radii is adiabatic 'heating' of pre-existing turbulence in the inflow. This assumption is similar to the underlying assumption of our solution that the dominant thermal heating mechanism is compression of the CGM inflow, rather than other heating sources such as feedback.

In a rotating inflow, turbulence may also be induced by the shear between adjacent shells. Radial displacements due to such turbulent motions are not subject to restoring Coriolis forces, since the non-perturbed solution is angular momentum conserving (Fig. 4) and hence the epicyclic frequency κ is zero. Balbus, Hawley & Stone (1996) showed that for a rotationally dominated disc with $\kappa = 0$ such turbulence develops with an e-folding time roughly equal to an orbit time. Given that hot CGM inflows onto Milky Way-like galaxies complete $\lesssim 2$ orbits before accretion (Fig. 6 with $t_{\rm cool}/t_{\rm ff} \approx 10$) it is unclear if shear-induced turbulence has sufficient time to develop.

As a preliminary test of the effect of turbulence on our hot rotating CGM solution, we run another simulation with similar ICs as in our fiducial simulation, to which we add a turbulent velocity field with amplitude $\sigma_{\rm turb}(t=0) = 30\,{\rm km\,s^{-1}}$ and a lognormal power spectrum peaking at a wavelength of 50 kpc and a logarithmic width of 1. Fig. 8 compares the results of this simulation after steady state is achieved with the results of the fiducial simulation shown in Figs 1–5. The top panel shows that adding turbulence increases the density fluctuations in the hot inflow, though they are still below unity at $t < t(10^5\,{\rm K})$. The bottom panel demonstrates the effect of turbulence on the specific

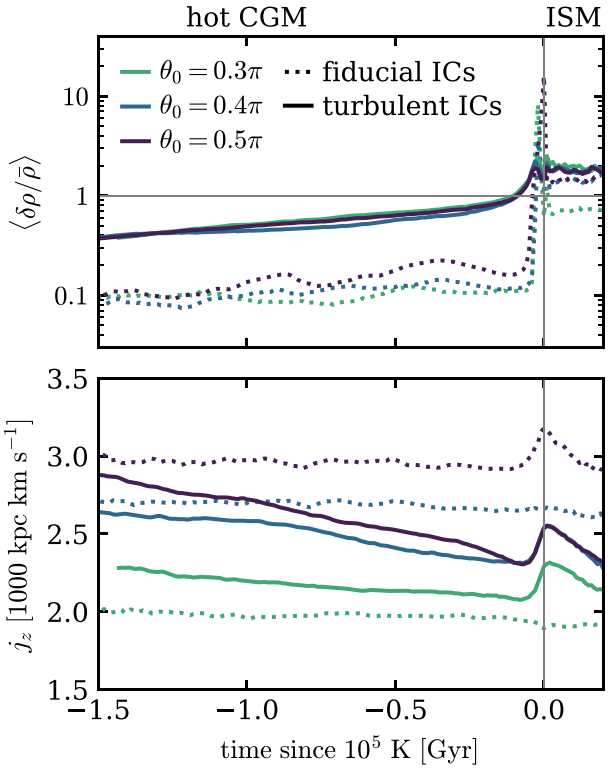

Figure 8. The effect of turbulence on hot rotating CGM inflows. The panels show density fluctuations (top) and specific angular momentum (bottom) along flowlines, versus time, since the hot CGM cools and accretes onto the ISM. Dashed lines denote the simulation with fiducial initial conditions (ICs) shown also in Figs 1–5, while solid lines denote a simulation with turbulent ICs. Line colour denotes the initial polar angle of the flowline as in Fig. 4. Note the mild angular momentum loss along flowlines in the turbulent simulation, in contrast with the constant angular momentum in the fiducial simulation.

angular momentum in the flow. The turbulent simulation shows a smaller difference in j_z between different flowlines than in the fiducial simulation, likely as a result of angular momentum transfer between flowlines. Also evident is the mild ($\lesssim 20$ per cent) decrease in j_z in the turbulent simulation over the last 1.5 Gyr prior to cooling, in contrast with the constant j_z in the fiducial simulation. This is potentially a result of transport of angular momentum outward during the inflow due to the turbulent viscosity between adjacent shells. Fig. 8 thus implies that turbulence, at the strength explored, has only a mild effect on the angular momentum content of the inflow, and specifically $\gtrsim 80$ per cent of the angular momentum in the inflowing hot CGM accretes onto the ISM.[3]

The development of turbulence in hot and rotating CGM inflows also affects the angular momentum distribution of accreting gas, since a large $\sigma_{\rm turb}$ necessary implies a broad angular momentum distribution. Hafen et al. (2022) argued that a narrow angular momentum distribution in accreting gas may be necessary for the formation of thin disc galaxies seen in the low-redshift Universe. This points to the importance of understanding turbulence in hot rotating CGM. We defer a detailed analysis to future work.

[3]The turbulent simulation has $\kappa \approx 0.2$ at $r \gtrsim R_{\rm c,\,max}$, in contrast with $\kappa = 0$ in the fiducial simulation. This finite κ is potentially sufficient to prevent any further development of hydrodynamic turbulence due to restoring Coriolis forces (Balbus et al. 1996).

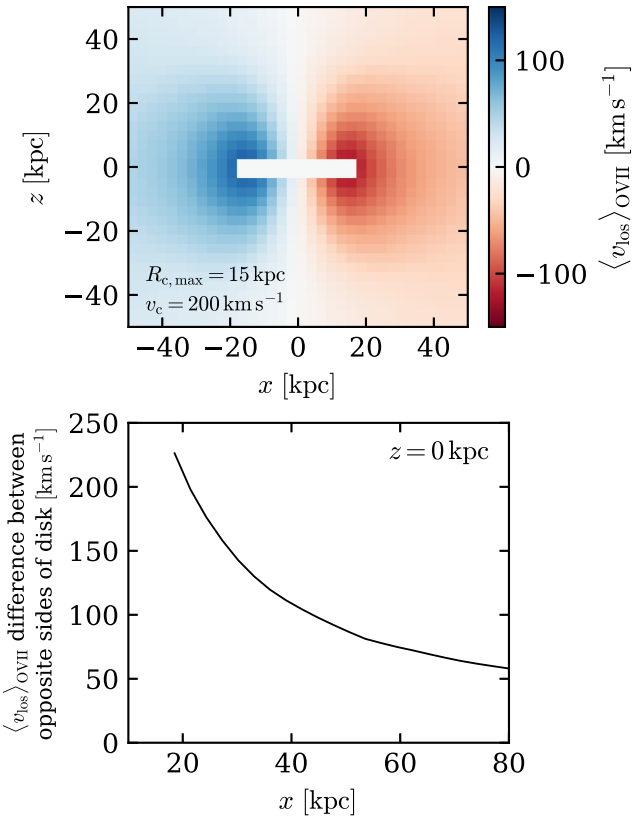

Figure 9. Top: predicted centroid shift of the O VII 0.56 keV emission line in a hot rotating CGM inflow feeding a disc galaxy. CGM rotation assumed to be viewed edge-on. Pixel size is 3 kpc × 3 kpc, corresponding to 15 arcsec resolution at a distance of 40 Mpc. The calculation is based on the fiducial simulation, with the central disc masked. Bottom: difference between line-of-sight velocity at opposite sides of the disc, in the mid-plane. Detecting the predicted $v_\phi \sim r^{-1}$ rotation profile in the hot CGM would support the hypothesis that it is inflowing.

4.3 Magnetic fields

The contraction and rotation in hot rotating CGM inflows is expected to enhance magnetic fields present at the outer radius of the inflow. In Appendix D, we estimate this enhancement using the rotating inflow solution derived above, assuming ideal magnetohydrodynamics (MHD) and ignoring potential dynamical effects of the magnetic field on the flow. Defining r_0 as the outer radius of the inflow, and assuming an isotropic seed field $B_r(r_0) = B_\theta(r_0) = B_\phi(r_0) \equiv B_0$, we find that

$$\frac{B_r}{B_0} = \left(\frac{r}{r_0}\right)^{-2},$$
$$\frac{B_\theta}{B_0} = \left(\frac{v_r r}{v_0 r_0}\right)^{-1},$$
$$\frac{B_\phi}{B_0} = \sqrt{2}\frac{t_{cool}}{t_{ff}}\frac{r_0^2 R_{c,max}}{r^3}\sin\theta, \quad (53)$$

where we also defined $v_0 \equiv v_r(r_0)$. The values of B_r/B_0, B_θ/B_0, and B_ϕ/B_0 are accurate up to corrections of order $(R_{c,\,max}/r)^2$.

The enhancement of the magnetic field in equation (53) can be compared to the enhancement in a non-rotating spherical inflow, which was derived by Shapiro (1973). They found $B_r \propto r^{-2}$ and $B_\theta \propto B_\phi \propto (v_r r)^{-1}$, which can be understood intuitively as a result of conservation of magnetic flux through patches moving with the flow. Rotation thus mainly affects the enhancement of B_ϕ, due to the winding of the field. Equation (53) shows that the enhancement of B_ϕ is a product of $(t_{cool}/t_{ff} \cdot R_{c,\,max}/r)$ and $(r_0/r)^2$, where the former tracks the number of radians rotated by the inflow (equation 44) and the latter tracks the contraction of an inflowing shell.

For $r_0/R_{c,\,max} \sim 6$ and $t_{cool}/t_{ff} \sim 6$ as expected in the hot Milky Way CGM (Section 2), equation (53) suggests an increase in B_ϕ of order ∼200 by the time the hot gas reaches $R_{c,\,max}$, just prior to accreting onto the galaxy. For comparison, the thermal pressure increases over the same range of radii as $P(R_{c,\,max})/P(r_0) \approx (R_{c,\,max}/r_0)^{-3/2} \sim 15$ (equation 10), and thus the ratio of thermal to magnetic pressure $\beta \propto P/B^2$ is expected to decrease by a large factor of ∼3000. Current upper limits on the magnetic field in the inner CGM of $\sim L^\star$ galaxies at $z \lesssim 0.3$ suggest magnetic pressure is subdominant to the thermal pressure ($\beta > 1$), at least along the major axis where most of the accretion is expected (Prochaska et al. 2019; Lan & Prochaska 2020; Heesen et al. 2023). It thus follows that if the hot CGM is accreting as suggested in this work, seed magnetic fields are sufficiently small that they do not dominate even after the large enhancement induced by contraction and rotation.

The eventual cooling of the inner hot CGM onto the ISM will further enhance B. Fig. 4(f) suggests that the gas density increases by a factor of ∼1000 as it cools, which would increase B by a further factor $\sim 1000^{2/3} = 100$ in the limit of ideal MHD. Another potentially interesting implication of the hot CGM solution concerns the development of turbulence due to the magnetic-rotational instability (MRI). The MRI amplitude growth rate is $\sim\Omega$ (e.g. Balbus & Hawley 1998; Masada & Sano 2008), so the result that $\int \Omega dt \approx t_{cool}/t_{ff}$ (Fig. 6, equation 44) implies that prior to accretion MRI can grow by $e^{t_{cool}/t_{ff}}$, that is, a factor of 10^4 for $t_{cool}/t_{ff} \approx 10$. The solution may thus change considerably as t_{cool}/t_{ff} exceeds some critical value where MRI becomes fully developed. We defer analysis of accretion via magnetic hot rotating CGM inflows to future work.

5 OBSERVATIONAL IMPLICATIONS

In this section, we discuss several observational signatures of hot and rotating CGM inflows. While it would be challenging to detect the predicted slow radial velocities of a few tens of km s^{-1} (equation 10), the predicted rotation velocities are faster, reaching $v_c \sim 200$ km s^{-1}, and indeed evidence for such fast hot gas rotation has been detected in the Milky Way CGM (Hodges-Kluck, Miller & Bregman 2016). Since an inflow imparts a specific rotation profile in the hot gas which is flatter ($v_\phi \sim r^{-1}$, equation 23) than the rotation profile expected prior to the development of an inflow ($v_\phi \sim r^{-0.5}$, Sharma et al. 2012a; Pezzulli et al. 2017; Sormani et al. 2018), measuring the rotation profile could be used to support or rule out the existence of inflows in the hot gas.

The hot gas rotation pattern can potentially be detected directly using X-ray emission line centroiding (Section 5.1), or indirectly, by identifying the lower densities and higher temperatures along the rotation axis relative to the mid-plane (Sections 5.2 and 5.3). The latter indirect signature would however have to be distinguished from qualitatively similar trends induced by feedback (Nica et al. 2022; Truong et al. 2021, 2023; Yang et al. 2024).

Given the idealized nature of the solution, signal strength estimates below are at the order of magnitude level. More realistic calculations based on cosmological simulations would be a useful next step.

5.1 Measuring hot gas rotation using line centroiding

Hodges-Kluck et al. (2016) analysed the centroids of 37 O VII absorption lines in the Milky Way CGM, in the context of a

phenomenological hot CGM model with $n_{\rm H} \propto r^{-1.5}$ and uniform inflow and rotational velocities. They deduced $v_r = -15 \pm 20\,{\rm km\ s^{-1}}$ and $v_\phi = 180 \pm 41\,{\rm km\ s^{-1}}$, or $v_r/v_{\rm c} = -0.06 \pm 0.08$ and $v_\phi = 0.75 \pm 0.17$ for a circular velocity of $v_{\rm c} = 240\,{\rm km\ s^{-1}}$ measured near the Sun. These values are comparable to those expected in hot rotating inflows near the disc, since $v_\phi/v_{\rm c} \approx R_{\rm c,\,max}/r$ and $v_r/v_{\rm c} \approx t_{\rm ff}/t_{\rm cool}$ (Figs 2, equations 41 and 10). Specifically, we calculate the O VII absorption-averaged v_ϕ and v_r in our fiducial simulation, along sightlines starting at $(R, z) = (8\,{\rm kpc}, 0\,{\rm kpc})$ with the same distribution of Galactic latitudes and longitudes as in the Popescu et al. (2004). The projection is done on a snapshot after the simulation converged onto a steady state. Line emissivity is calculated based on the gas density and temperature in the simulation using the PYXSIM package (ZuHone & Hallman 2016).[4] Pixel size in this panel is 3 kpc, corresponding to the planned 15 arcsec resolution of the proposed line emission mapper probe (LEM, Kraft et al. 2022) for a target at a distance of 40 Mpc.[5] The bottom panel shows the line centroid difference between the approaching and receding sides of the CGM, in the mid-plane. This difference reaches 200 km s^{-1} near the disc, higher than the planned centroiding accuracy of $\lesssim 70\,{\rm km\ s^{-1}}$ planned for LEM. X-ray telescopes with high spectral resolution may thus be able to measure the rotation velocity profile in the hot CGM, and test whether it is consistent with the inflow solution.

5.2 Angle dependence of X-ray emission and temperature

Angular momentum support induces deviations from spherical symmetry in the hot CGM density and temperature (Section 3.4, Fig. 5). These are potentially detectable by measuring the dependence of CGM X-ray emission on the 'azimuthal angle', defined as the orientation of the sightline with respect to the galaxy major axis (e.g. Kacprzak et al. 2015). The top panel in Fig. 10 shows the predicted soft X-ray surface brightness versus azimuthal angle and impact parameter $R_\perp$, assuming CGM rotation is oriented edge-on in the plane of the sky. Surface brightness is calculated using PYXSIM on the NGC 891-like simulation used also in Fig. 9. The figure shows that the soft X-ray brightness ($\propto n_{\rm H}^2$) increases towards the major axis at small $R_\perp$, since rotation induces a higher CGM density near the mid-plane (equation 41, Fig. 5).

The bottom panel in Fig. 10 shows the luminosity ratio of the O VIII Lyα 0.65 keV and O VII Heα 0.56 keV emission lines. The ratio increases towards the minor axis, by up to 75 per cent at $R_\perp = 30$ kpc. This follows since this emission line ratio depends mainly on CGM temperature which is higher along the rotation axis (see Fig. 5).

5.3 Dispersion measure

Observations of the dispersion measures to pulsars in the Magellanic clouds and towards extragalactic fast radio bursts (FRBs) constrain electron column densities in the CGM (e.g. Anderson & Bregman 2010; Prochaska & Zheng 2019; Ravi et al. 2023; Williams, Khan & McQuinn 2023). Fig. 11 plots predicted dispersion measures for an external galaxy and for the Milky Way CGM, based on our fiducial simulation. For external galaxy sightlines we assume an inclination $i = 77^\circ$ similar to M31, and integrate the electron density along sightlines with different impact parameters $R_\perp$ and different azimuthal angles. We start and end the integration at a spherical

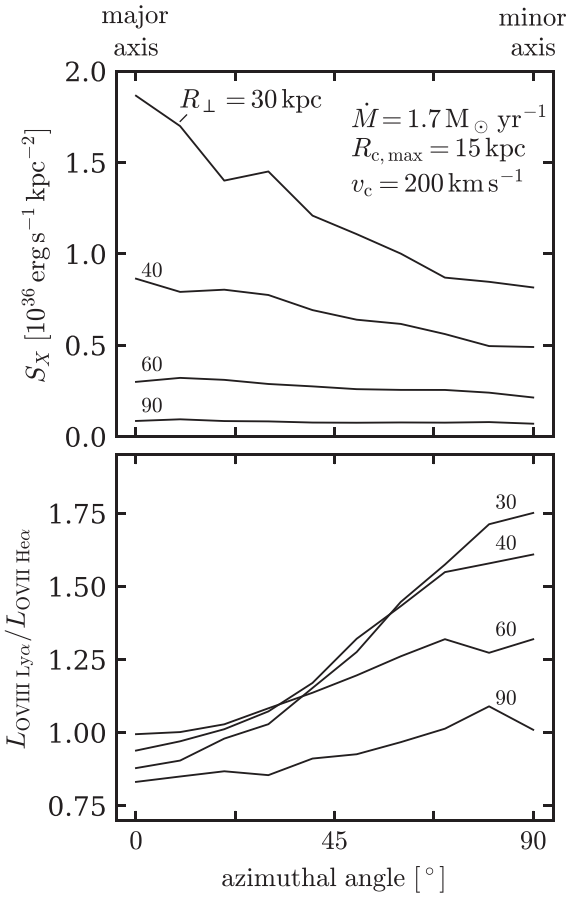

Figure 10. X-ray emission from hot rotating inflows versus azimuthal angle (defined as the sightline orientation relative to galaxy major axis), for an edge-on galaxy. Different lines denote different impact parameters. Calculations are based on the fiducial simulation. Top: predicted soft X-ray surface brightness. Surface brightness decreases with angle due to the lower densities near the rotation axis induced by angular momentum support. Bottom: O VIII Lyα/O VII Heα emission line ratio. The ratio increases with angle due to higher temperatures near the rotation axis (see Fig. 5).

radius $r = 100\,{\rm kpc}$, roughly equal to $r_{\rm cool}$ (Section 2.1) beyond which the hot inflow solution does not apply. Fig. 11 shows that the highest dispersion measures of $\approx 30\,{\rm cm^{-3}\,pc}$ are found at small impact parameters and small azimuthal angles where densities are highest (see equation 41). For Milky Way sightlines the dispersion measures were calculated by integrating from $(R, z) = (8\,{\rm kpc}, 1\,{\rm kpc})$ out to $r = 100\,{\rm kpc}$, for different Galactic latitudes b and Galactic longitudes l. We start at $z = 1$ kpc to avoid the contribution of the cool disc, while the exact choice of outer limit does not significantly affect the result since most of the contribution comes from small radii. The predicted dispersion measures are $12 - 18\,{\rm cm^{-3}\,pc}$ and increase towards lower b, again due to higher densities near the disc plane.

Fig. 11 also shows the upper limit of $23\,{\rm cm^{-3}\,pc}$ for the CGM dispersion measure from Anderson & Bregman (2010), deduced based on sightlines to pulsars in the LMC (Large Magellanic Cloud, though note caveat in Ravi et al. 2023, which may imply this upper limit is too restrictive). This upper limit is consistent with our prediction of $14\,{\rm cm^{-3}\,pc}$ in sightlines with $|b| = 30^\circ$ and $l = 270^\circ$ when integrating out to an LMC distance of $r = 50\,{\rm kpc}$.

[4] Version 4.2.0

[5] At smaller redshifts the target line emission would be drowned by line emission from the Milky Way, see Kraft et al. (2022).

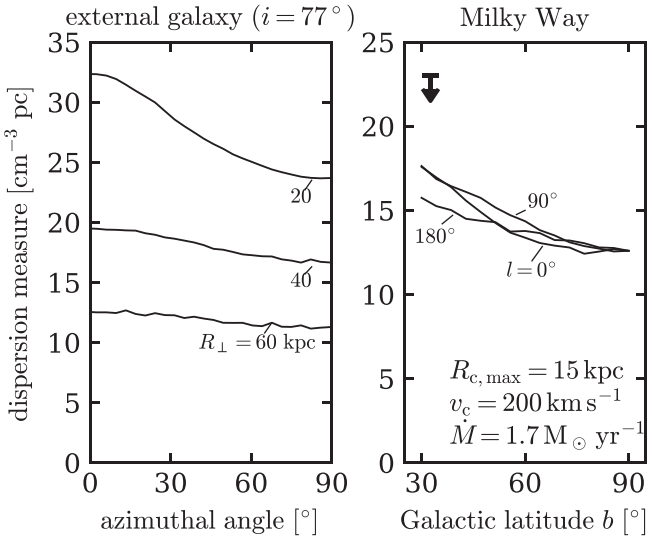

Figure 11. Predicted dispersion measures from a CGM forming a hot rotating inflow, for sightlines through an external galaxy CGM (left, assuming M31-like inclination) and through the Milky Way CGM (right), based on the fiducial simulation. External galaxy sightlines are given as a function of impact parameter and azimuthal angle, while Milky Way sightlines as a function of Galactic coordinates. Integration is limited to $r < 100$ kpc where a hot inflow is possible. The upper limit from Anderson & Bregman (2010), derived from sightlines to pulsars in the LMC, is noted in the right panel. The decrease in dispersion measure with increasing azimuthal angle and b is due to the lower densities near the rotation axis.

6 DISCUSSION

6.1 Comparison to previous hot CGM models

In the solution described in this work the hot CGM is inflowing, since ongoing feedback heating is assumed to be small relative to radiative losses. This is in contrast with the typical assumption employed by models of the low-redshift CGM, where the hot CGM phase is static due to feedback heating balancing radiative losses (e.g. Sharma et al. 2012a; Faerman et al. 2017, 2020; Voit et al. 2017). Several models have accounted also for rotation in the hot CGM (Pezzulli et al. 2017; Sormani et al. 2018; Afruni, Pezzulli & Fraternali 2022), though also in these latter models the gas is assumed not to flow in the radial direction. A third possibility is that feedback heating exceeds radiative losses, and the hot CGM forms an outflow (e.g. Thompson et al. 2016; Schneider et al. 2020, though note these studies neglected a pre-existing CGM). As the mechanics of CGM heating by stellar and AGN feedback are currently not well understood, and existing X-ray constraints do not rule out an inflow as in the ICM (see Introduction), it is currently unclear which of these three paradigms is more accurate.

Despite the qualitative distinction between hot inflows explored here and static hot CGM models explored by previous studies, both types of models satisfy similar hydrostatic equilibrium constraints. This follows since the inflow solution is highly subsonic, and hence deviations from hydrostatic equilibrium in the radial direction are small, of order $(t_{\rm cool}/t_{\rm ff})^{-2}$. Indeed, these deviations are neglected in the analytic solution derived in Section 2.4. The assumption of an inflow however enforces conservation of mass, energy, and angular momentum between adjacent shells (equations 20–22), while there are no similar constraints on static models. The allowed space of inflowing hot CGM solutions is thus significantly smaller than that of static solutions. For example, deducing the entropy profile in static models requires employing another assumption, such that the entropy is independent of radius (Faerman et al. 2020), or that $t_{\rm cool}/t_{\rm ff}$ is independent of radius (Voit et al. 2017). In the inflow solution derived here the entropy profile is fully determined by the flow equations.

Inflow solutions are also more specific than static models in the predicted rotation profile of the hot CGM. Sormani et al. (2018) used several constraints to derive $v_\phi(r, \theta)$ in their static hot CGM model, mainly the typical CGM angular momentum distribution in cosmological simulations and OVII absorption-based estimates of Milky Way CGM rotation from Hodges-Kluck et al. (2016). These constraints are however rather sparse and leave considerable freedom for different choices of $v_\phi(r, \theta)$, as discussed in Stern et al. (2021b, see fig. 13 there).

6.2 Accretion via hot inflows versus 'precipitation'

Accretion onto the Milky Way and nearby spirals is likely dominated either by 'precipitation', where local thermal instability in the hot phase creates $\sim 10^4$ K gas clumps which lose buoyancy and accrete (e.g. Fall & Rees 1985; Maller & Bullock 2004; Voit et al. 2015; Armillotta, Fraternali & Marinacci 2016), or by the hot $\sim 10^6$ K inflows discussed in this work (see Introduction). Both accretion modes would be considered 'hot accretion' in the context of the classic distinction between the hot and cold accretion modes, since they both originate in the hot phase of the CGM (e.g. Nelson et al. 2013). However, in the scenario studied here the CGM inflow remains at $\sim 10^6$ K down to a cylindrical radius $R_{\rm c,max} \sim 15$ kpc and height of $\sim$ kpc above the mid-plane, at which point all the hot gas cools and joins the ISM, rather than just a subset of localized clouds. Hot inflows are thus a type of 'quiet accretion' (Putman et al. 2012) – accretion which becomes accessible to cool gas observations only when it cannot be kinematically distinguished from pre-existing disc gas.

We note that at outer CGM radii of $r \gtrsim r_{\rm cool} \sim 100$ kpc a hot inflow is not expected since cooling times are long (Section 2.1), so any infall would likely be dominated by cool $\sim 10^4$ K gas. This cool inflow at large radii can potentially join a hot inflow at small CGM radii if the cool clouds are disrupted by hydrodynamic instabilities (e.g. Afruni et al. 2023; Tan et al. 2023).

6.3 Hot inflows require that CGM of typical $\sim L^*$ spirals have previously expanded due to feedback

In steady state, we expect a CGM inflow rate of $\dot{M} \approx 0.6$ SFR, which is $\approx 1\,\mathrm{M_\odot\ yr^{-1}}$ for the Milky Way (Section 2.1). We show here that if this $\dot{M}$ originates in a hot inflow, the CGM density must be lower than expected in a baryon-complete halo.

Integrating the density profile in equation (10) out to the virial radius and solving for $\dot{M}$, we get:

$$\dot{M} = 6.6 \left(\frac{M_{\rm CGM}}{10^{11}\,\mathrm{M_\odot}}\right)^2 \left(\frac{R_{\rm CGM}}{300\,\mathrm{kpc}}\right)^{-3} v_{\rm c,200}^{-2} \Lambda_{-22}\,\mathrm{M_\odot\ yr^{-1}}\,, \quad (54)$$

where we normalized $M_{\rm CGM}$ by the the baryon-complete CGM mass of $0.16 M_{\rm halo} - M_{\rm galaxy} = 10^{11}\,\mathrm{M_\odot}$ for $M_{\rm halo} = 10^{12}\,\mathrm{M_\odot}$ and a galaxy mass $M_{\rm galaxy} = 6 \times 10^{10}\,\mathrm{M_\odot}$. The CGM size $R_{\rm CGM}$ is normalized by $r_{\rm vir} \approx 300$ kpc. This predicted $\dot{M}$ is higher than the $\approx 1\,\mathrm{M_\odot\ yr^{-1}}$ required to sustain star formation in local discs. It thus follows that for local discs to be fed by hot CGM inflows, gas originally associated with the halo must have expanded beyond $r_{\rm vir}$. Such an expanded CGM is supported by recent thermal Sunyaev–Zeldovich (tSZ) maps of nearby spirals, which indicate that the baryon budget of the halo is spread over a size of $R_{\rm CGM} \gtrsim 500$ kpc (Bregman et al. 2022). Using

this larger estimate of $R_{\rm CGM}$ in equation (54) would suggest $\dot{M} \lesssim 1.5\,{\rm M}_\odot$, consistent with observed SFRs. The large $R_{\rm CGM}$ deduced by Bregman et al. (2022) thus supports the scenario that local disc galaxies are fed by hot CGM inflows.

There is however an inherent challenge in a scenario where discs are fed by an inflow from an expanded hot CGM. An expanding CGM is apparently contradictory to an inflowing CGM, and requires feedback heating to dominate radiative cooling, in contrast with the above assumption that feedback heating is subdominant. This apparent contradiction can be circumvented if the inflow and expansion are separated either in time or in space. For example, it is plausible that feedback was strong high redshift causing the CGM to expand, and has since subsided so the hot CGM develops an inflow at low redshift. Such an evolution in feedback strength is predicted by FIRE simulations of Milky Way mass galaxies (Muratov et al. 2015; Faucher-Giguère 2018; Pandya et al. 2021; Stern et al. 2021b), and is also consistent with observed stellar winds which are strong in $z \sim 2$ galaxies but weak in typical $\sim L^\star$ galaxies at $z \sim 0$ (Heckman & Thompson 2017). Alternatively, black hole feedback or stellar feedback which occur in 'bursts' separated by more than ~ 1 Gyr would allow a hot inflow to develop between bursts, since this timescale is the cooling time in the inner CGM on which a hot inflow develops. A third possibility is that feedback mainly heats the outer CGM, allowing the inner CGM to form an inflow. While this may seem counter-intuitive, it is potentially possible if feedback is focused on the rotation axis at small CGM radii and isotropizes only at large CGM radii, thus allowing the hot inner CGM to inflow from the mid-plane. Another option is that feedback energy is propagated by weak shocks or sound waves which dissipate and dump heat only in the outer CGM. The distribution of feedback energy in space and time has been explored extensively in the context of the ICM (e.g. Yang & Reynolds 2016; Martizzi et al. 2019; Donahue & Voit 2022), but less so in the context of the CGM. A thorough exploration would allowing understanding under which conditions the hot CGM inflow scenario is viable.

6.4 Disc–halo interface

The cooling layer of the hot inflow solution found above, in which the gas temperature drops from $\approx 2 \times 10^6$ to $\lesssim 10^4$ K, occurs at $|z| \lesssim 0.5$ kpc in our fiducial simulation (see Fig. 1 and Fig. C1). This simulated cool layer is thinner than the 'extraplanar' layers of neutral and ionized $\sim 10^4$ K gas detected around nearby spirals, which extend to $|z| \approx$ several kpc (e.g. Gaensler et al. 2008; Sancisi et al. 2008). Also, the mass flow rate through this layer in our simulation is $\dot{M} \approx 1\,{\rm M}_\odot\,{\rm yr}^{-1} \sim$ SFR, in contrast with $\sim 10 \times$ SFR in observed extraplanar gas layers (e.g. Marasco et al. 2019).

Extraplanar gas is often assumed to be dominated by fountain flows (Shapiro & Field 1976; Bregman 1980), in which cool clouds driven upward by feedback penetrate into the hot CGM and then fall back onto the disc (Fraternali & Binney 2006, 2008; Marasco et al. 2012; Fraternali 2017). Fountain flows thus both increase the vertical extent of the cool gas and the total mass circulating through the extraplanar gas layer. These models usually assume the hot CGM is not inflowing, which as mentioned above requires a delicate balance between feedback heating and cooling, a balance especially hard to achieve in the inner CGM where cooling times are short (see also discussion of this issue in Sormani & Sobacchi 2019). It would thus be beneficial to study how fountain flows interact with the inflowing hot CGM solution derived herein. Specifically, one could use the angular momentum structure of a hot inflow derived above to understand how fountain orbits are affected by angular momentum exchange with the hot CGM, an interaction that has observable implications (e.g. Fraternali 2017). Also it would be useful to understand how this fountain – hot CGM interaction affects the accretion rate profile onto the disc (compare Fig. 7 above with fig. 9 in Marasco et al. 2012).

We note that some of the above studies argued that fountain flows are required for accretion from the hot CGM, since they trigger cool cloud condensation in the hot gas. Our simulations show that the hot CGM cools and can fuel star formation even without fountain flows. Cooling in our solution is however a steady process which affects the entire hot inflow as it reaches the disc–halo interface, rather than a result of condensation of localized cool clouds.

6.5 Truncation of thin discs at $R \approx R_{\rm c,\,max}$

For discs fed by hot rotating inflows, $R_{\rm c,\,max}$ corresponds to the maximum cylindrical radius at which gas cools and accretes onto the ISM (Fig. 7). This is also evident as a sharp edge of the cool gas disc at $R = R_{\rm c,\,max}$ in the temperature maps shown in Fig. 1, and is a result of hot CGM inflows cooling and accreting only when $v_\phi = v_{\rm c}$ (Fig. 4d). Similar behaviour has been identified in FIRE cosmological simulations of low-redshift Milky Way mass galaxies which are also fed by hot rotating inflows (Hafen et al. 2022; Trapp et al. 2022).

The predicted maximum accretion radius at $R_{\rm c,\,max}$ is similar to the observed truncation radius $R_{\rm trunc}$ of nearby disc galaxies, beyond which the stellar and H I surface densities drop (e.g. van der Kruit 2007). Such a truncation is observed in 60 per cent − 80 per cent of thin discs at $R_{\rm trunc} \approx 3.5$–$4R_{\rm d}$ where $R_{\rm d}$ is the disc scale length (Kregel, van der Kruit & de Grijs 2002; Comerón et al. 2012; Martín-Navarro et al. 2012).[6] When an H I warp is present it also often starts at $R \approx R_{\rm trunc}$ (van der Kruit 2007). Using $R_{\rm trunc} = 3.5R_{\rm d} \approx 0.04r_{\rm vir}$ based on the $R_{\rm d}$–$r_{\rm vir}$ relation from Kravtsov (2013) and $R_{\rm c,\,max} \approx 0.05r_{\rm vir}$ (equation 15), we get $R_{\rm c,\,max} \approx R_{\rm trunc}$. It is thus plausible that observed disc truncations are ultimately a result of the abrupt cut in gas accretion beyond this radius, as suggested by Trapp et al. (2022). In the context of hot rotating CGM inflows this maximum radius of accretion is set by $R_{\rm c,\,max}$.

7 SUMMARY

In this work, we derive an axisymmetric, steady-state solution for hot and rotating CGM inflows, focusing on Milky Way mass galaxies at $z \sim 0$. We demonstrate that such accretion flows transition from a spherical, hot ($\sim 10^6$ K) radial inflow to a cool ($\lesssim 10^4$ K) disc supported by rotation. This cooling occurs at the disc–halo interface, within a cylindrical radius equal to the maximum circularization radius of the flow $R_{\rm c,max} \sim 15$ kpc and at heights $|z| \lesssim$ kpc above the disc. Such hot inflows are expected in the CGM if radiative cooling has dominated over feedback heating for a cooling timescale. This condition is easier to satisfy at inner CGM radii where cooling times can be substantially shorter than the *Hubble* time.

We find both a new analytic solution for hot inflows in the slow rotation limit, which is valid in the limit $(r/R_{\rm c,\,max})^2 \gg 1$ (Section 2.4), and a numerical solution applicable also at $r \lesssim R_{\rm c,\,max}$ (Section 3). These solutions provide an idealized version of the hot CGM inflows identified by Hafen et al. (2022) in FIRE simulations of Milky

[6]The derived fraction of thin discs which exhibit a truncation is based on discs observed edge-on, since at low inclination stellar haloes make the truncation harder to observe (Martín-Navarro et al. 2014).

Way mass galaxies at $z \sim 0$. The main properties of these solutions can be summarized as follows:

(i) Due to a balance between radiative cooling and compressive heating, hot inflows remain hot down to where they become rotationally supported, at which point the inflow and compressive heating stop and the entire flow cools (Figs 1–4). Hot inflows thus differ qualitatively from 'precipitation' in which accretion proceeds via a subset of clouds formed due to thermal instability.

(ii) Angular momentum of accreting gas is conserved during the inflow due to the axisymmetry of the solution (Fig. 4j), yielding an accretion flow which feeds the disc mainly from its outskirts (Fig. 7, Section 2.6). Conservation of angular momentum also suggests $v_\phi \propto r^{-1}$ in the hot CGM at radii $R_{\rm c,\,max} < r < r_{\rm cool}$ (Fig. 2), flatter than the $v_\phi \propto r^{0.5} - r^{0.7}$ suggested by non-radiative cosmological simulations (Sharma et al. 2012b). This predicted rotation profile could potentially be detected with X-ray microcalorimeters which can centroid emission lines to $\lesssim 100\,{\rm km\ s^{-1}}$ (Fig. 9).

(iii) Gas accreting via hot CGM inflows revolves $\approx t_{\rm cool}/t_{\rm ff}$ radians prior to accretion (Fig. 6), where $t_{\rm cool}/t_{\rm ff}$ is estimated in gas just outside the galaxy ($\sim$6 in the Milky Way). This in contrast with only $\approx$1 radian of revolution in gas accreting via cold flows. Enhancement of magnetic fields and development of turbulence in the hot CGM thus likely depend on the value of $t_{\rm cool}/t_{\rm ff}$ (Sections 4.2 and 4.3).

(iv) Rotational support induces deviations from spherical symmetry in the density and temperature structure of hot CGM inflows (Fig. 5), qualitatively similar to the rotating but radially static models of Sormani et al. (2018). These deviations may be detectable with X-ray telescopes (Fig. 10), or with dispersion measures derived from FRB surveys (Fig. 11).

(v) Observed SFRs in local spirals constrain typical hot inflow accretion rates to $\dot{M} \lesssim 1 - 2\,{\rm M_\odot\ yr^{-1}}$. In the absence of ongoing feedback heating as assumed here, such accretion rates require that the halo baryon budget is spread over $\gtrsim 2r_{\rm vir}$ in order to reduce CGM densities and cooling rates. Bregman et al. (2022) recently reported evidence for such expanded CGM using tSZ maps around nearby spirals.

(vi) By analysing the centroids of OVII absorption lines in the Milky Way CGM, Hodges-Kluck et al. (2016) deduced a hot CGM rotation velocity of $v_\phi \approx 180 \pm 40\,{\rm km\ s^{-1}}$ and a marginal inflow velocity of $v_r \approx -15 \pm 20\,{\rm km\ s^{-1}}$. Both values are consistent with those expected if the hot Milky Way CGM forms a rotating inflow (Section 5.1).

The solution derived herein provides an analytic basis for understanding the structure of the inner hot CGM, in the presence of angular momentum and radiative cooling. It would be beneficial for future studies to further develop this framework with additional relevant physical processes and complications applicable to the real Universe, including polar-angle dependent feedback heating, fountain flows, turbulence (briefly discussed in Section 4.2), magnetic fields (Section 4.3), and misalignments between the rotation axes of the hot CGM, disc, and dark matter halo.

ACKNOWLEDGEMENTS

We thank the anonymous referee for a highly detailed and insightful report that significantly improved the paper. JS thanks S. Peng Oh and M. Voit for useful discussions. JS was supported by the Israel Science Foundation (grant no. 2584/21). CAFG was supported by NSF through grants AST-2108230, AST-2307327, and CAREER award AST-1652522; by NASA through grants 17-ATP17-0067 and 21-ATP21-0036; by STScI through grants HST-GO-16730.016-A and JWSTAR-03252.001-A; and by CXO through grant TM2-23005X. This work was supported in part by a Simons Investigator award from the Simons Foundaton (EQ) and by NSF grant AST-2107872. JSB was supported by the National Science Foundation (NSF) grant AST-1910965 and NASA grant 80NSSC22K0827. The computations in this work were run at facilities supported by the Scientific Computing Core at the Flatiron Institute, a division of the Simons Foundation.

DATA AVAILABILITY

The simulation data underlying this article will be shared on reasonable request to the corresponding author (JS). A public version of the GIZMO simulation code is available http://www.tapir.caltech.edu/phopkins/Site/GIZMO.html.

REFERENCES

Afruni A., Pezzulli G., Fraternali F., 2022, MNRAS, 509, 4849
Afruni A., Pezzulli G., Fraternali F., Grønnow A., 2023, MNRAS, 524, 2351
Agertz O. et al., 2007, MNRAS, 380, 963
Anderson M. E., Bregman J. N., 2010, ApJ, 714, 320
Anderson M. E., Gaspari M., White S. D. M., Wang W., Dai X., 2015, MNRAS, 449, 3806
Anderson M. E., Churazov E., Bregman J. N., 2016, MNRAS, 455, 227
Armillotta L., Fraternali F., Marinacci F., 2016, MNRAS, 462, 4157
Armillotta L., Fraternali F., Werk J. K., Prochaska J. X., Marinacci F., 2017, MNRAS, 470, 114
Balbus S. A., Hawley J. F., 1998, Rev. Mod. Phys., 70, 1
Balbus S. A., Soker N., 1989, ApJ, 341, 611
Balbus S. A., Hawley J. F., Stone J. M., 1996, ApJ, 467, 76
Barnabè M., Ciotti L., Fraternali F., Sancisi R., 2006, A&A, 446, 61
Bertschinger E., 1989, ApJ, 340, 666
Birnboim Y., Dekel A., 2003, MNRAS, 345, 349
Bland-Hawthorn J., Gerhard O., 2016, ARA&A, 54, 529
Bogdán Á., Bourdin H., Forman W. R., Kraft R. P., Vogelsberger M., Hernquist L., Springel V., 2017, ApJ, 850, 98
Bondi H., 1952, MNRAS, 112, 195
Bregman J. N., 1980, ApJ, 236, 577
Bregman J. N., Hodges-Kluck E., Qu Z., Pratt C., Li J.-T., Yun Y., 2022, ApJ, 928, 14
Bullock J. S., Dekel A., Kolatt T. S., Kravtsov A. V., Klypin A. A., Porciani C., Primack J. R., 2001, ApJ, 555, 240
Cassen P., Pettibone D., 1976, ApJ, 208, 500
Chadayammuri U., Bogdán Á., Oppenheimer B. D., Kraft R. P., Forman W. R., Jones C., 2022, ApJ, 936, L15
Comerón S. et al., 2012, ApJ, 759, 98
Comparat J. et al., 2022, A&A, 666, A156
Cowie L. L., Fabian A. C., Nulsen P. E. J., 1980, MNRAS, 191, 399
Das S., Mathur S., Gupta A., Nicastro F., Krongold Y., Null C., 2019, ApJ, 885, 108
DeFelippis D., Genel S., Bryan G. L., Nelson D., Pillepich A., Hernquist L., 2020, ApJ, 895, 17
Donahue M., Voit G. M., 2022, Phys. Rep., 973, 1
Fabian A. C., Nulsen P. E. J., Canizares C. R., 1984, Nature, 310, 733
Fabian A. C., Reynolds C. S., Taylor G. B., Dunn R. J. H., 2005, MNRAS, 363, 891
Faerman Y., Sternberg A., McKee C. F., 2017, ApJ, 835, 52
Faerman Y., Sternberg A., McKee C. F., 2020, ApJ, 893, 82
Fall S. M., Rees M. J., 1985, ApJ, 298, 18
Faucher-Giguère C.-A., 2018, MNRAS, 473, 3717
Fielding D. B., McKee C. F., Socrates A., Cunningham A. J., Klein R. I., 2015, MNRAS, 450, 3306
Fielding D., Quataert E., McCourt M., Thompson T. A., 2017, MNRAS, 466, 3810
Fielding D. B. et al., 2020, ApJ, 903, 32

Fox A. J., Richter P., Ashley T., Heckman T. M., Lehner N., Werk J. K., Bordoloi R., Peeples M. S., 2019, ApJ, 884, 53
Fraternali F., 2017, in Fox A., Davé R., eds, Astrophysics and Space Science Library Vol. 430, Gas Accretion onto Galaxies. Springer International Publishing AG, Cham, p. 323
Fraternali F., Binney J. J., 2006, MNRAS, 366, 449
Fraternali F., Binney J. J., 2008, MNRAS, 386, 935
Gaensler B. M., Madsen G. J., Chatterjee S., Mao S. A., 2008, Publ. Astron. Soc. Aust., 25, 184
Gurvich A. B. et al., 2023, MNRAS, 519, 2598
Hafen Z. et al., 2022, MNRAS, 514, 5056
Heckman T. M., Thompson T. A., 2017, in Alsabti A. W., Murdin P., eds, Handbook of Supernovae. Springer International Publishing AG, Cham, p. 2431
Heesen V. et al., 2023, A&A, 670, L23
Heitsch F., Putman M. E., 2009, ApJ, 698, 1485
Hodges-Kluck E. J., Miller M. J., Bregman J. N., 2016, ApJ, 822, 21
Hopkins P. F., 2015, MNRAS, 450, 53
Hopkins P. F. et al., 2018, MNRAS, 480, 800
Huscher E., Oppenheimer B. D., Lonardi A., Crain R. A., Richings A. J., Schaye J., 2021, MNRAS, 500, 1476
Kacprzak G. G., Muzahid S., Churchill C. W., Nielsen N. M., Charlton J. C., 2015, ApJ, 815, 22
Kamphuis P. et al., 2022, A&A, 668, A182
Kaufmann T., Mayer L., Wadsley J., Stadel J., Moore B., 2006, MNRAS, 370, 1612
Kaufmann T., Bullock J. S., Maller A. H., Fang T., Wadsley J., 2009, MNRAS, 396, 191
Kraft R. et al., 2022, preprint (arXiv:2211.09827)
Kravtsov A. V., 2013, ApJ, 764, L31
Kregel M., van der Kruit P. C., de Grijs R., 2002, MNRAS, 334, 646
Krumholz M. R., Burkhart B., Forbes J. C., Crocker R. M., 2018, MNRAS, 477, 2716
Lan T.-W., Prochaska J. X., 2020, MNRAS, 496, 3142
Li Y., Bregman J., 2017, ApJ, 849, 105
Li J.-T., Wang Q. D., 2013, MNRAS, 435, 3071
Li J.-T., Crain R. A., Wang Q. D., 2014, MNRAS, 440, 859
Lilly S. J., Carollo C. M., Pipino A., Renzini A., Peng Y., 2013, ApJ, 772, 119
Maller A. H., Bullock J. S., 2004, MNRAS, 355, 694
Marasco A., Fraternali F., Binney J. J., 2012, MNRAS, 419, 1107
Marasco A. et al., 2019, A&A, 631, A50
Martín-Navarro I. et al., 2012, MNRAS, 427, 1102
Martín-Navarro I., Trujillo I., Knapen J. H., Bakos J., Fliri J., 2014, MNRAS, 441, 2809
Martizzi D., Quataert E., Faucher-Giguère C.-A., Fielding D., 2019, MNRAS, 483, 2465
Masada Y., Sano T., 2008, ApJ, 689, 1234
Mathews W. G., Bregman J. N., 1978, ApJ, 224, 308
McCourt M., Sharma P., Quataert E., Parrish I. J., 2012, MNRAS, 419, 3319
McDonald M., Gaspari M., McNamara B. R., Tremblay G. R., 2018, ApJ, 858, 45
McQuinn M., Werk J. K., 2018, ApJ, 852, 33
Miller M. J., Bregman J. N., 2015, ApJ, 800, 14
Muratov A. L., Kereš D., Faucher-Giguère C.-A., Hopkins P. F., Quataert E., Murray N., 2015, MNRAS, 454, 2691
Murray N., Chang P., 2015, ApJ, 804, 44
Murray D. W., Chang P., Murray N. W., Pittman J., 2017, MNRAS, 465, 1316
Narayan R., Fabian A. C., 2011, MNRAS, 415, 3721
Narayan R., Medvedev M. V., 2001, ApJ, 562, L129
Nelson D., Vogelsberger M., Genel S., Sijacki D., Kereš D., Springel V., Hernquist L., 2013, MNRAS, 429, 3353
Nelson D. et al., 2019, MNRAS, 490, 3234
Nica A., Oppenheimer B. D., Crain R. A., Bogdán Á., Davies J. J., Forman W. R., Kraft R. P., ZuHone J. A., 2022, MNRAS, 517, 1958
Oppenheimer B. D., 2018, MNRAS, 480, 2963
Pandya V. et al., 2021, MNRAS, 508, 2979
Pezzulli G., Fraternali F., Binney J., 2017, MNRAS, 467, 311
Popescu C. C., Tuffs R. J., Kylafis N. D., Madore B. F., 2004, A&A, 414, 45
Prochaska J. X., Zheng Y., 2019, MNRAS, 485, 648
Prochaska J. X. et al., 2019, ApJS, 243, 24
Putman M. E., Peek J. E. G., Joung M. R., 2012, ARA&A, 50, 491
Quataert E., Narayan R., 2000, ApJ, 528, 236
Ramachandran P., Varoquaux G., 2011, Comput. Sci. Eng., 13, 40
Ravi V. et al., 2023, preprint (arXiv:2301.01000)
Robertson B., Goldreich P., 2012, ApJ, 750, L31
Rodríguez-Puebla A., Behroozi P., Primack J., Klypin A., Lee C., Hellinger D., 2016, MNRAS, 462, 893
Roškar R., Debattista V. P., Brooks A. M., Quinn T. R., Brook C. B., Governato F., Dalcanton J. J., Wadsley J., 2010, MNRAS, 408, 783
Sancisi R., Fraternali F., Oosterloo T., van der Hulst T., 2008, A&AR, 15, 189
Schneider E. E., Ostriker E. C., Robertson B. E., Thompson T. A., 2020, ApJ, 895, 43
Schönrich R., Binney J., 2009, MNRAS, 396, 203
Shapiro S. L., 1973, ApJ, 185, 69
Shapiro P. R., Field G. B., 1976, ApJ, 205, 762
Sharma P., McCourt M., Quataert E., Parrish I. J., 2012a, MNRAS, 420, 3174
Sharma S., Steinmetz M., Bland-Hawthorn J., 2012b, ApJ, 750, 107
Sormani M. C., Sobacchi E., 2019, MNRAS, 486, 215
Sormani M. C., Sobacchi E., Pezzulli G., Binney J., Klessen R. S., 2018, MNRAS, 481, 3370
Springel V., di Matteo T., Hernquist L., 2005, MNRAS, 361, 776
Stern J., Fielding D., Faucher-Giguère C.-A., Quataert E., 2019, MNRAS, 488, 2549
Stern J., Fielding D., Faucher-Giguère C.-A., Quataert E., 2020, MNRAS, 492, 6042
Stern J. et al., 2021a, MNRAS, 507, 2869
Stern J. et al., 2021b, ApJ, 911, 88
Stevens A. R. H., Lagos C. d. P., Contreras S., Croton D. J., Padilla N. D., Schaller M., Schaye J., Theuns T., 2017, MNRAS, 467, 2066
Stewart K. R., Brooks A. M., Bullock J. S., Maller A. H., Diemand J., Wadsley J., Moustakas L. A., 2013, ApJ, 769, 74
Stewart K. R. et al., 2017, ApJ, 843, 47
Su K.-Y. et al., 2019, MNRAS, 487, 4393
Su K.-Y. et al., 2020, MNRAS, 491, 1190
Sweet P. A., 1950, MNRAS, 110, 548
Tan B., Oh S. P., Gronke M., 2023, MNRAS, 520, 2571
Tassoul J.-L., 2007, Stellar Rotation. Cambridge Univ. Press, Cambridge
Thompson T. A., Quataert E., Zhang D., Weinberg D. H., 2016, MNRAS, 455, 1830
Trapp C. W. et al., 2022, MNRAS, 509, 4149
Truong N., Pillepich A., Nelson D., Werner N., Hernquist L., 2021, MNRAS, 508, 1563
Truong N. et al., 2023, MNRAS, 525, 1976
van der Kruit P. C., 2007, A&A, 466, 883
Voit G. M., Donahue M., O'Shea B. W., Bryan G. L., Sun M., Werner N., 2015, ApJ, 803, L21
Voit G. M., Meece G., Li Y., O'Shea B. W., Bryan G. L., Donahue M., 2017, ApJ, 845, 80
Wang E., Lilly S. J., 2022, ApJ, 927, 217
White S. D. M., Rees M. J., 1978, MNRAS, 183, 341
Wiersma R. P. C., Schaye J., Smith B. D., 2009, MNRAS, 393, 99
Williams I. M., Khan A., McQuinn M., 2023, MNRAS, 520, 3626
Yang H. Y. K., Reynolds C. S., 2016, ApJ, 829, 90
Yang T., Davé R., Cui W., Cai Y.-C., Peacock J. A., Sorini D., 2024, MNRAS, 527, 1612
Yu S. et al., 2021, MNRAS, 505, 889
Yu S. et al., 2023, MNRAS, 523, 6220
ZuHone J. A., Hallman E. J., 2016, Astrophysics Source Code Library, record ascl:1608.002
ZuHone J. A. et al., 2023, preprint (arXiv:2307.01269)

APPENDIX A: θ-DEPENDENT ROTATION PROFILES

In this section, we give analytic solutions for hot CGM inflows in the slow-rotation limit as derived in Section 2.4, for different assumptions on how the gas rotates at large radii. This dependence of Ω_1 on θ is set by the outer boundary condition of the solution and is parametrized using the function $F(\theta)$ (see equation 26):

$$\Omega_1 = \frac{v_c}{R_{c,max}} \left(\frac{r}{R_{c,max}} \right)^{-2} F(\theta) \,, \tag{A1}$$

where $F(\pi/2) = 1$. The solution in the main text (equation 41) is for $F(\theta) = 1$. For $F = \sin\theta$, we find

$$\begin{aligned} f_P &= \frac{3}{8}\sin^4(\theta) - \frac{3}{10}, \\ f_\rho &= \frac{15}{8}\sin^4(\theta) - \frac{7}{10}, \\ f_T &= -\frac{3}{2}\sin^4(\theta) + \frac{2}{5} \,. \end{aligned} \tag{A2}$$

For $F(\theta) = \sin^2\theta$, we get

$$\begin{aligned} f_P &= \frac{1}{4}\sin^6(\theta) - \frac{1}{5}, \\ f_\rho &= \frac{19}{12}\sin^6(\theta) - \frac{7}{15}, \\ f_T &= -\frac{4}{3}\sin^6(\theta) + \frac{4}{15} \,, \end{aligned} \tag{A3}$$

while for $F(\theta) = \sin^3\theta$, we get

$$\begin{aligned} f_P &= \frac{3}{16}\sin^8(\theta) - \frac{16}{105}, \\ f_\rho &= \frac{23}{16}\sin^8(\theta) - \frac{16}{45}, \\ f_T &= -\frac{5}{4}\sin^8(\theta) + \frac{64}{315} \,. \end{aligned} \tag{A4}$$

APPENDIX B: DIMENSIONLESS FLOW EQUATIONS

The flow equations (18)–(22) can be dedimensionalized, if we approximate the cooling function as a power law $\Lambda = \Lambda_{10^6}(T/10^6)^{-l}$. We define the dimensionless variables as

$$\begin{aligned} r' &\equiv \frac{r}{R_{c,max}}, \\ \{v_r', v_\theta', v_\phi', c_s'\} &\equiv \frac{\{v_r, v_\theta, v_\phi, c_s\}}{v_c}, \\ \rho' \equiv \frac{\rho}{\rho^\star}, &\qquad P' \equiv \frac{P}{\frac{3}{5}\rho^\star v_c^2}, \end{aligned} \tag{B1}$$

with the density normalization equal to

$$\rho^\star = \frac{9 m_p^2 v_c^{3+2l}}{10 X^2 \Lambda_{10^6} R_{c,max}}, \tag{B2}$$

where $m_p/X = \rho/n_H$ (m_p and X are the proton mass and hydrogen mass fraction, respectively). This gives for the flow equations

$$\begin{aligned} \frac{\partial P'}{\partial r'} &= -\frac{\rho'}{r'} + \frac{v_\phi'^2}{r'}, \\ \frac{\partial P'}{\partial \theta} &= -\rho' v_\phi'^2 \frac{\cos\theta}{\sin\theta}, \\ v_r' \frac{\partial (v_\phi' r' \sin\theta)}{\partial r'} + v_\theta' \frac{\partial (v_\phi' r' \sin\theta)}{r' \partial\theta} &= 0, \\ \frac{1}{r'^2}\frac{\partial (\rho' v_r' r'^2)}{\partial r'} + \frac{1}{r'\sin\theta}\frac{\partial (\rho' v_\theta' r'^2)}{\partial\theta} &= 0, \\ v_r' \frac{\partial (\ln K)}{\partial r'} + v_\theta' \frac{\partial (\ln K)}{r' \partial\theta} &= \rho' c_s'^{-2(1+l)}. \end{aligned} \tag{B3}$$

These dimensionless equations imply that changing $R_{c,\,max}$ and/or v_c does not change the solution beyond a scaling, if the gas density is also scaled by $\rho^\star$.

The value of $\rho^\star$ is related to the critical accretion rate $\dot{M}_{crit}$ discussed in Stern et al. (2020):

$$4\pi R_{c,max}^2 \rho^\star v_c = \frac{18\pi m_p^2 v_c^{4+2l} R_{c,max}}{5 X^2 \Lambda_{10^6}} = \dot{M}_{crit}(R_{c,max}, v_c) \tag{B4}$$

(see equation 8 there).[7] When $\dot{M} = \dot{M}_{crit}$, the ratio t_{cool}/t_{ff} equals unity at $r = R_{c,\,max}$ in the spherical solution (equation 10), and hence the sonic radius of the flow coincides with the circularization radius. The relation (B4) between $\rho^\star$ and $\dot{M}_{crit}$ thus implies that changing $R_{c,\,max}$ and/or v_c does not change the solution beyond a scaling, if $\dot{M}$ is also scaled by $\dot{M}_{crit}$. Hot rotating inflows thus form a family of solutions characterized by a single parameter, $\dot{M}/\dot{M}_{crit}$, up to a scaling of the physical dimensions.

APPENDIX C: GAS PROPERTIES NEAR THE TIME OF COOLING AND ACCRETION

Fig. C1 plots gas properties along flowlines as in Fig. 4, zoomed in on times near $t(10^5\,\mathrm{K})$, which corresponds to the time of accretion from the hot CGM onto the cool ISM.

[7] In Stern et al. (2020), we effectively assumed $l = 0$ and neglected a factor of 9/10 in the calculation of $\dot{M}_{crit}$.

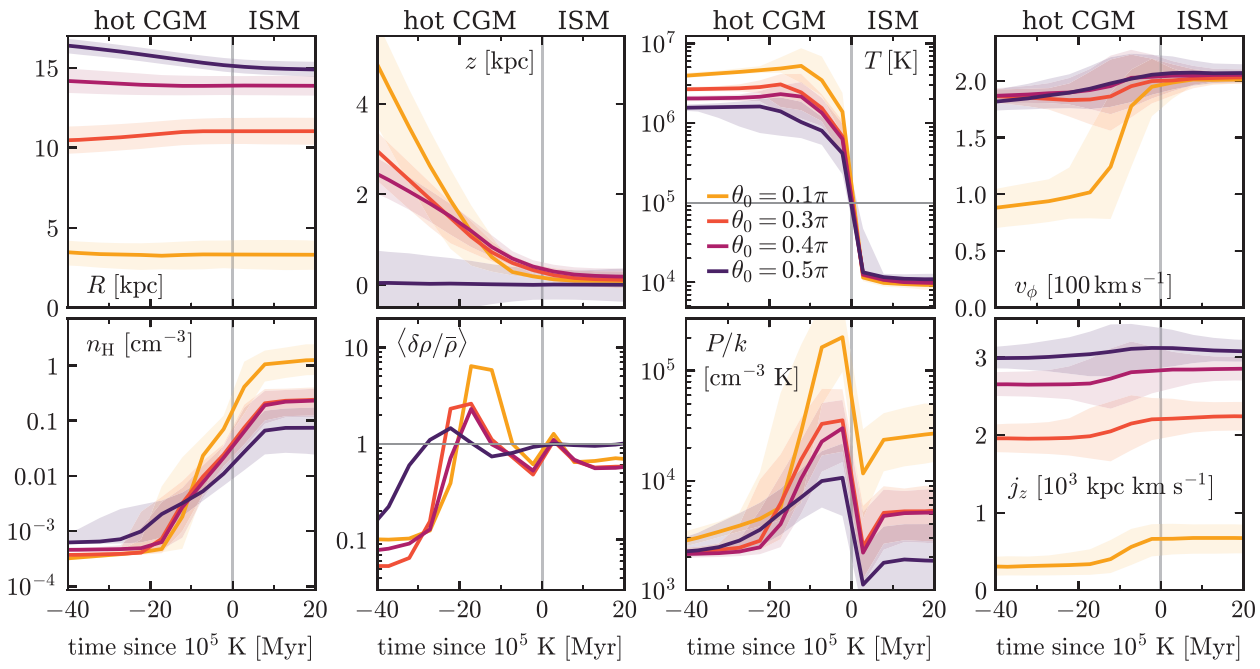

Figure C1. Gas properties along flowlines as in Fig. 4, zoomed-in on times near the time of cooling. Colour denotes flowlines originating at different polar angles θ_0. Solid lines and bands correspond to medians and 16th–84th percentiles. Top panels show R, z, T, and v_ϕ, while bottom panels show n_H, $\langle\delta\rho/\bar{\rho}\rangle$, P/k, and j_z. The R and z panels demonstrate that cooling occurs just above the disc, at the 'disc–halo interface'. Except for the mid-plane flowline ($\theta_0 = 0.5\pi$) the flow direction is almost vertical at the shown times, with z decreasing by $2-4$ kpc and R changing by $\lesssim 0.5$ kpc. At ≈ 20 Myr prior to cooling gas densities start to increase while density fluctuations become significant. This rapidly shortens the cooling time which allows the eventual drop in temperature to occur over a short timescale of ~ 10 Myr, as can be seen in the T panel.

APPENDIX D: MAGNETIC FIELDS IN HOT AND ROTATING CGM INFLOWS

In this section, we derive an estimate of the magnetic field B in a rotating hot CGM inflow, by assuming ideal MHD conditions and neglecting any potential dynamical effects of the field on the flow. We employ the analytic solution in equation (41), disregarding terms of order $(R_{\rm c,\,max}/r)^2$ or higher. Combined with the assumption of axisymmetry and steady state we then have $v_\theta = \partial/\partial\phi = \partial/\partial t = 0$, and the ideal MHD equations for the magnetic field

$$\nabla\cdot\boldsymbol{B} = 0, \quad \nabla\times(\boldsymbol{v}\times\boldsymbol{B}) = \frac{\partial\boldsymbol{B}}{\partial t} \tag{D1}$$

reduce to

$$\begin{aligned}
\frac{1}{r^2}\frac{\partial}{\partial r}(r^2 B_r) &= -\frac{1}{r\sin\theta}\frac{\partial}{\partial\theta}(B_\theta\sin\theta),\\
\frac{\partial}{\partial r}(v_r B_\theta r) &= 0,\\
\frac{\partial}{\partial\theta}(v_r B_\theta\sin\theta) &= 0,\\
\frac{\partial}{\partial r}(v_\phi B_r r - v_r B_\phi r) &= -\frac{\partial(v_\phi B_\theta)}{\partial\theta}\,.
\end{aligned} \tag{D2}$$

Assuming for simplicity that the field is isotropic at the outer radius of the inflow r_0 with $B_r(r_0) = B_\theta(r_0) = B_\phi(r_0) \equiv B_0$, the first two equations imply

$$B_r = B_0\left(\frac{r}{r_0}\right)^{-2}, \tag{D3}$$

$$B_\theta = B_0\left(\frac{v_r r}{v_r(r_0)r_0}\right)^{-1}. \tag{D4}$$

Equations (D3) and (D4) are the same as in a non-rotating, spherical inflow solution (Shapiro 1973). To solve for B_ϕ, we note that the right-hand side in the last equation in (D2) equals zero. This follows from the third condition in equation (D2) together with $v_\phi \propto \sin\theta$ and $\partial v_r/\partial\theta = 0$ [equation (41), up to corrections of order $(r/R_{\rm c,\,max})^{-2}$]. It thus follows that

$$\frac{\partial(v_\phi B_r r - v_r B_\phi r)}{\partial\theta} = 0\,, \tag{D5}$$

and integrating we get

$$v_\phi B_r r - v_r B_\phi r = B_0 r_0(v_\phi(r_0) - v_r(r_0))\,. \tag{D6}$$

Using equation (D3) for B_r then gives

$$B_\phi = B_0\left(\frac{v_r r}{v_r(r_0)r_0}\right)^{-1}\left[1 + \frac{v_\phi r_0}{v_r(r_0)r} - \frac{v_\phi(r_0)}{v_r(r_0)}\right]. \tag{D7}$$

For $v_\phi = 0$, equation (D7) reduces to $B_\phi \propto (v_r r)^{-1}$, as in the Shapiro (1973) non-rotating solution. For finite v_ϕ, the second term in the brackets scales as $\approx r^{-3/2}$ (since at large radii $v_\phi \sim r^{-1}$ and $v_r \sim r^{-0.5}$), and hence for r somewhat smaller than r_0 this term will dominate the other two terms. We thus get

$$B_\phi \approx B_0\frac{v_\phi}{v_r}\left(\frac{r}{r_0}\right)^{-2} = \sqrt{2}\frac{t_{\rm cool}}{t_{\rm ff}}\frac{r_0^2 R_{\rm c,max}}{r^3}\sin\theta\,, \tag{D8}$$

where in the last approximation, we use $v_\phi = v_{\rm c}R_{\rm c,\,max}\sin\theta/r$, $v_r = r/t_{\rm cool}$, and $t_{\rm ff} = \sqrt{2}r/v_{\rm c}$. Specifically, at $r \approx R_{\rm c,\,max}$ just prior to

accretion we get

$$\frac{B_\phi(R_{\rm c,max})}{B_0} \approx \sqrt{2}\frac{t_{\rm cool}}{t_{\rm ff}}(R_{\rm c,max})\left(\frac{R_{\rm c,max}}{r_0}\right)^{-2}\sin\theta\ . \tag{D9}$$

This result suggests that the enhancement of B_ϕ at $R_{\rm c,\,max}$ is a product of $t_{\rm cool}/t_{\rm ff}(R_{\rm c,\,max})$ and $(r_0/R_{\rm c,\,max})^2$, where the former tracks the number of radians rotated by the inflow (equation 44) and the latter tracks the contraction of an inflowing shell.

This paper has been typeset from a TEX/LATEX file prepared by the author.